

MASSACHUSETTS INST OF TECH LEXINGTON LINCOLN LAB
SOLID STATE RESEARCH, 1979:3,(U)
AUG 79 A L MCWHORTER F.

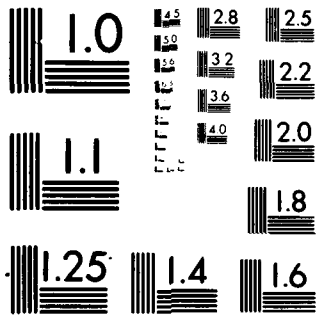
F19628-7B-C-0002

ESD-TR-79-210

NL

$$\left\{ \begin{array}{l} N \\ \Delta_{\text{max}}^{\text{max}} \end{array} \right\}$$

END
DATE
FILMED
6-80
DTIC



MICROCOPY RESOLUTION TEST CHART

NATIONAL BUREAU OF STANDARDS-1963-A

12

A078676

LEVEL

III

ADA 084270

See 1473
on back page

3

Solid State Research

1979

Prepared
under Electronic Systems Division Contract F19628-78-C-0002 by

Lincoln Laboratory

MASSACHUSETTS INSTITUTE OF TECHNOLOGY

LEXINGTON, MASSACHUSETTS



Approved for public release; distribution unlimited.

DTIC
ELECTE
MAY 20 1980

S

D

E

80 5 19 220

DOC FILE COPY

The work reported in this document was performed at Lincoln Laboratory, a center for research operated by Massachusetts Institute of Technology, with the support of the Department of the Air Force under Contract F19628-78-C-0002.

This report may be reproduced to satisfy needs of U.S. Government agencies.

The views and conclusions contained in this document are those of the contractor and should not be interpreted as necessarily representing the official policies, either expressed or implied, of the United States Government.

This technical report has been reviewed and is approved for publication.

FOR THE COMMANDER

Raymond L. Loiselle
Raymond L. Loiselle, Lt. Col., USAF
Chief, ESD Lincoln Laboratory Project Office

Non-Lincoln Recipients

PLEASE DO NOT RETURN

Permission is given to destroy this document
when it is no longer needed.

MASSACHUSETTS INSTITUTE OF TECHNOLOGY
LINCOLN LABORATORY

SOLID STATE RESEARCH

QUARTERLY TECHNICAL SUMMARY REPORT

1 MAY - 31 JULY 1979

ISSUED 14 JANUARY 1980

Accession For	
NTIS GRA&I	<input checked="checked" type="checkbox"/>
DDC TAB	<input type="checkbox"/>
Unannounced	<input type="checkbox"/>
Justification	
By _____	
Distribution/	
Availability Codes	
Dist	Avail and/or special
A	

Approved for public release; distribution unlimited.

LEXINGTON

MASSACHUSETTS

ABSTRACT

This report covers in detail the solid state research work of the Solid State Division at Lincoln Laboratory for the period 1 May through 31 July 1979. The topics covered are Solid State Device Research, Quantum Electronics, Materials Research, Microelectronics, and Analog Device Technology. Funding is primarily provided by the Air Force, with additional support provided by the Army, ARPA, NSF, and DOE.

CONTENTS

Abstract	iii
Introduction	vii
Reports on Solid State Research	x
Organization	xix
I. SOLID STATE DEVICE RESEARCH	1
A. Fabrication of Ohmic Contacts on p-InP Using Ion Implantation and Laser Annealing	1
B. Ti-Diffused Optical Waveguide Devices in LiNbO ₃	4
II. QUANTUM ELECTRONICS	9
A. Differential-Absorption Measurements of Atmospheric CO Using a Frequency-Doubled CO ₂ LIDAR	9
B. Advances in Transition-Metal-Doped Lasers	13
C. Effects of Narrow Free-Spectral-Range Etalons on Mode-Locked Lasers	14
D. Characteristics of External Cavity (Ga,Al)As Diode Lasers	19
E. Atomic Transition Lasers Based on Two-Photon Dissociation of Metal Tri-iodide Vapors	23
F. Ultraviolet Laser Photodeposition of Metal Atoms	25
G. Tunable Submillimeter Sources Applied to Kinetics and Relaxation Processes in the First Excited ν ₃ State of CH ₃ F	28
III. MATERIALS RESEARCH	33
A. Growth of GaAs Epilayers on Large-Grained GaAs Substrates	33
B. GaAs Solar Cells With High Resistance to 1-MeV Electron Radiation	37
IV. MICROELECTRONICS	43
A. Photolithographic Mask Evaluation by Electrical Testing	43
B. Enhanced Substrate Contacts via Laser-Annealed Back-Side Ion Implantation Into Silicon Devices	45
C. Charge-Coupled Devices: Imagers	46
V. ANALOG DEVICE TECHNOLOGY	49
A. Efficient Conversion of Surface Acoustic Waves in Shallow Gratings to Bulk Plate Modes	49
B. Fabrication of Josephson-Junction Devices	52

INTRODUCTION

I. SOLID STATE DEVICE RESEARCH

Ohmic contacts on p-InP with average specific contact resistances as low as $5 \times 10^{-5} \Omega\text{-cm}^2$ have been obtained by using a combination of Q-switched laser annealing, ion implantation, and evaporated Au without microalloying. These unusually low contact resistances are important for many semiconductor devices, including diode lasers, which require minimum resistance heating for high efficiency and reliability.

As a first step in the development of high-speed guided-wave electrooptic A/D converters, Ti-diffused LiNbO₃ directional couplers, branching waveguides, and electrooptic interferometric modulators were successfully fabricated and tested. The interferometric modulators had a 17-dB extinction ratio and exhibited better performance for this type of device than has been reported previously.

II. QUANTUM ELECTRONICS

Single-ended remote sensing measurements of the atmospheric concentration of CO have been made out to a distance of 2.5 km using differential absorption of line-tunable, frequency-doubled CO₂-laser radiation. Diurnal variations of CO concentration in the range from 0.15 to 1 ppm were seen over a 500-m path.

CW operation of a Co:MgF₂ laser has been achieved for the first time, and continuous tuning over a 1300-cm^{-1} range from 1.63 to 2.08 μm has been demonstrated. In two different experiments, a Ni:MgF₂ laser has been operated on a single frequency with 20 mW of output power and has been Q-switched to yield 140 W of peak power, with an output-energy-density extraction of 1 J/cm^3 .

The effect of etalon frequency selectivity on homogeneously broadened mode-locked lasers in the limit of low finesse and narrow free spectral range has been calculated. The etalon does not affect the mode-locked pulse width, but modulates the frequency spectrum and causes small secondary pulses. Significant perturbation occurs when the etalon discrimination is one to two orders of magnitude less than the depth of mode-locking modulation.

By using a stable, single-mode, tunable external-cavity semiconductor laser, the effects of spectral and spatial gain hole burning on the laser spectrum have been investigated. In addition, this laser has been mode-locked using microwave injection modulation.

Visible laser action on atomic transitions of Ga, In, Al, and Bi has been obtained by using an ArF excimer laser to photodissociate vapors of the corresponding metal tri-iodides. An output energy of 0.24 mJ at 417.2 nm and an energy efficiency of 2.9 percent have been obtained with Ga.

Experiments with UV photodeposition of metals have shown the efficacy of a buffer-gas additive in localizing the deposition process. In addition, the deposition rate has been measured and shown to increase linearly with laser fluence and the absorption coefficient of the parent gas.

The infrared-submillimeter double-resonance experiment, which uses the generation and detection of tunable submillimeter radiation in Schottky-diode mixers, has been extended to pulsed measurements. This has permitted observations of rapid time-dependent phenomena in vibrationally excited CH_3F .

III. MATERIALS RESEARCH

As a step in the development of technology for producing efficient GaAs solar cells on low-cost substrates, the chemical vapor deposition of GaAs epitaxial layers on large-grained GaAs substrates has been investigated in order to determine the dependence of growth rate, surface morphology, and impurity doping on crystallographic orientation. Variations in surface topography from grain-to-grain can be minimized by adjusting the growth parameters, and variations in doping with Zn or S are small enough to be compatible with present techniques for fabricating shallow-homojunction GaAs cells on single-crystal substrates.

Shallow-homojunction GaAs solar cells have been found to exhibit superior resistance to 1-MeV electron radiation, indicating that such cells would be very resistant to the radiation of the space environment. By optimizing device design and fabrication procedure, it should therefore be possible to produce cells of this type as efficient power sources with long operating lifetimes for space applications.

IV. MICROELECTRONICS

A DC measurement technique has been developed to aid in the 100-percent inspection of chromium-on-glass photolithographic masks. These measurements detect the presence of chromium bridges between adjacent lines on masks used to define the metallization on the device. After the existence of a bridging defect has been detected, microscopic examination is used to locate the defect, and laser vaporization or spot etching is used to eliminate it.

Electrical activation of ion implants by laser annealing has been shown to be a tool for wafer rework at advanced stages of wafer fabrication in situations where conventional thermal processes are not possible. By using this technique, an ohmic contact has been fabricated to the back side of a wafer of commercially obtained, 512-stage, binary-reference, analog CCD correlator chips. These devices were difficult to test functionally as received, but the addition of the back-side ohmic contact allowed operation suitable for preliminary testing.

MgO/Au cermet films have been used to form integrated light shields to prevent illumination of the output register and detection circuitry of the CCD imaging devices being fabricated for the GEODSS (Ground Electro-Optical Deep Space Surveillance) Program. The MgO/Au films satisfy all the requirements for this light shield because of their high optical absorption, high resistivity, and ease of deposition and pattern definition.

V. ANALOG DEVICE TECHNOLOGY

Nearly 100-percent conversion of surface acoustic waves to bulk plate modes via normal-incidence gratings has been observed for surface waves of wavelength near the grating period. For a crystal with gratings on opposite faces, a surface wave on one face is efficiently coupled to a surface wave on the opposite face. A theory has been developed that can predict the transmission coefficients and the selected frequencies at which efficient conversion occurs.

Techniques for fabricating Josephson-junction devices have been developed. The basic junction structure consists of a niobium base electrode, a niobium oxide tunnel barrier, and a lead counterelectrode. A normal metal, aluminum, or an indium-gold alloy is employed in thin-film resistors.

REPORTS ON SOLID STATE RESEARCH

15 May through 15 August 1979

PUBLISHED REPORTS

Journal Articles

JA No.

- | | | | |
|------|---|---|---|
| 4853 | High Resolution Double Resonance Spectroscopy of SF ₆ | P. F. Moulton
A. Mooradian | In <u>Laser Induced Processes in Molecules</u> , edited by K. L. Kompa and S. D. Smith (Springer-Verlag, New York, 1979), p. 37 |
| 4872 | Wavenumbers, Line Strengths, and Assignments in the Doppler-Limited Spectrum of Formaldehyde from 2700 to 3000 cm ⁻¹ | L. R. Brown*
R. H. Hunt*
A. S. Pine | J. Mol. Spectrosc. <u>75</u> , 406 (1979) |
| 4877 | Energy Extraction from Metastable Excimers - Hg ₂ as an Energy Storage Medium | D. J. Ehrlich
R. M. Osgood, Jr. | IEEE J. Quantum Electron. <u>QE-15</u> , 301 (1979) |
| 4886 | Spectral Intensities in the ν_3 Bands of ¹² CH ₄ and ¹³ CH ₄ | M. Dang-Nhu*
A. S. Pine
A. G. Robiette* | J. Mol. Spectrosc. <u>77</u> , 57 (1979), DDC AD-A076741 |
| 4891 | Alkali-Metal Resonance-Line Lasers Based on Photodissociation | D. J. Ehrlich
R. M. Osgood, Jr. | Appl. Phys. Lett. <u>34</u> , 655 (1979), DDC AD-A073882 |
| 4897 | Linear Scan Control of Tunable Lasers Using a Scanning Fabry-Perot | M. J. Coulombe
A. S. Pine | Appl. Opt. <u>18</u> , 1505 (1979), DDC AD-A074034 |
| 4901 | Synthesis and Crystal Growth of CdGeP ₂ | P. Vohl | J. Electron. Mater. <u>8</u> , 517 (1979), DDC AD-A072372 |
| 4902 | Anomalous Noise Behavior in Wide-Bandwidth Photodiodes in Heterodyne and Background-Limited Operation | D. L. Spears
R. H. Kingston | Appl. Phys. Lett. <u>34</u> , 589 (1979), DDC AD-A074035 |
| 4906 | Higher-Order Nonlinear Processes in CdGeAs ₂ | H. Kildal
G. W. Iseler | Phys. Rev. B <u>19</u> , 5218 (1979) |
| 4913 | Laser Emission Study of the Pressure Dependence of the Energy Gap in Tellurium | A. S. Pine
N. Menyuk
G. Dresselhaus* | Solid State Commun. <u>31</u> , 187 (1979), DDC AD-A076744 |

*Author not at Lincoln Laboratory.

JA No.

- | | | | |
|------|--|---|---|
| 4920 | Ion-Implanted Laser-Annealed GaAs Solar Cells | J. C. C. Fan
R. L. Chapman
J. P. Donnelly
G. W. Turner
C. O. Bozler | Appl. Phys. Lett. <u>34</u> , 780
(1979), DDC AD-A073884 |
| 4930 | Crystallographic Orientation of Silicon on an Amorphous Substrate Using an Artificial Surface-Relief Grating and Laser Crystallization | M. W. Geis
D. C. Flanders
H. I. Smith | Appl. Phys. Lett. <u>35</u> , 71
(1979), DDC AD-A076745 |
| 4931 | A SAW/CCD Accumulating Correlator | D. L. Smythe
R. W. Ralston
E. Stern | Appl. Phys. Lett. <u>34</u> , 620
(1979), DDC AD-A073885 |
| 4933 | Planar Guarded Avalanche Diodes in InP Fabricated by Ion Implantation | J. P. Donnelly
C. A. Armiento
V. Diadiuk
S. H. Groves | Appl. Phys. Lett. <u>35</u> , 74
(1979), DDC AD-A076746 |
| 4936 | FM Mode-Locked $\text{Nd}_{0.5}\text{La}_{0.5}\text{P}_5\text{O}_{14}$ Laser | S. R. Chinn
W. K. Zwicker* | Appl. Phys. Lett. <u>34</u> , 847
(1979), DDC AD-A076426 |
| 4937 | Electroabsorption in GaInAsP | R. H. Kingston | Appl. Phys. Lett. <u>34</u> , 744
(1979), DDC AD-A074033 |
| 4946 | Laser Photodeposition of Metal Films with Microscopic Features | T. F. Deutsch
D. J. Ehrlich
R. M. Osgood, Jr. | Appl. Phys. Lett. <u>35</u> , 175
(1979), DDC AD-A076463 |
| 4949 | Ultraviolet Solid-State Ce:YLF Laser at 325 nm | D. J. Ehrlich
P. F. Moulton
R. M. Osgood, Jr. | Opt. Lett. <u>4</u> , 184 (1979) |
| 4962 | Four-Wave Interactions in Acoustoelectric Integrating Correlators | R. W. Ralston
E. Stern | Appl. Phys. Lett. <u>35</u> , 150
(1979), DDC AD-A076466 |

Meeting SpeechesMS No.

- | | | | |
|------|--|---|--|
| 4577 | High Na^+ -Ion Conductivity in $\text{Na}_5\text{YSi}_4\text{O}_{12}$ | H. Y-P. Hong
J. A. Kafalas
M. L. Bayard | <u>Proceedings of the 28th Power Sources Symposium</u>
(Electrochemical Society, Princeton, New Jersey, 1979), p. 1 |
| 4578 | NASICON, A New Solid Electrolyte for Na/S Batteries | J. A. Kafalas
H. Y-P. Hong | <u>Proceedings of the 28th Power Sources Symposium</u>
(Electrochemical Society, Princeton, New Jersey, 1979), p. 2 |

*Author not at Lincoln Laboratory.

MS No.

- | | | | |
|-------|--|---|---|
| 4753A | Emission Cross Section and Flashlamp-Excited $\text{NdP}_5\text{O}_{14}$ Laser at $1.32 \mu\text{m}$ | M. M. Choy*
W. K. Zwicker*
S. R. Chinn | Proc. Intl. Conf. on Lasers '78, Orlando, Florida, 11-15 December 1978, pp. 163-167 |
| 4756 | Properties of InP Doped with Fe, Cr or Co | G. W. Iseler | Chapter 2 in <u>Gallium Arsenide and Related Compounds</u> (St. Louis) 1978 (The Institute of Physics, London, 1979), pp. 144-153, DDC AD-A072404 |
| 4779 | Annealing of Se-Implanted GaAs and InP by Scanned Nd:YAG Laser Irradiation | J. C. C. Fan
J. P. Donnelly
C. O. Bozler
R. L. Chapman | Chapter 6 in <u>Gallium Arsenide and Related Compounds</u> (St. Louis) 1978 (The Institute of Physics, London, 1979), pp. 472-483, DDC AD-A072363 |
| 4953 | The Alignment of Masks and Substrates for X-ray Lithography | D. C. Shaver
D. C. Flanders | Proc. Lithography/Microscopy Beam Line Design Workshop, SSRL No. 79/02, Stanford University, 21-22 February 1979, pp. 131-142 |

* * * * *

UNPUBLISHED REPORTS

Journal ArticlesJA No.

- | | | | |
|------|--|--|--|
| 4895 | Extended Measurement and Analysis of the ν_3 Infrared Band of Methane | D. L. Gray*
A. G. Robiette*
A. S. Pine | Accepted by J. Mol. Spectrosc. |
| 4932 | Electron Paramagnetic Resonance in Ferrous Fluosilicate at Submillimeter Wavelengths | R. S. Rubins*
H. R. Fetterman | Accepted by J. Chem. Phys. |
| 4934 | Calculated and Measured Efficiencies of Shallow-Homojunction GaAs Solar Cells | J. C. C. Fan
C. O. Bozler
B. J. Palm | Accepted by Appl. Phys. Lett. |
| 4944 | Design and Development of a High-Speed Electrooptic A/D Converter | F. J. Leonberger
C. E. Woodward
D. L. Spears | Accepted by IEEE Trans. Circuits and Systems |
| 4947 | Solid Electrolytes Containing Both Mobile and Immobile Alkali Ions | H. Y-P. Hong | Accepted by J. Power Sources |
| 4948 | Efficient Conversion of Surface Acoustic Waves in Shallow Gratings to Bulk Plate Modes | J. Melngailis
H. A. Haus*
A. Lattes* | Accepted by Appl. Phys. Lett. |

*Author not at Lincoln Laboratory.

JA No.			
4963	Spectroscopy and Lasing in $K_5NdLi_2F_{10}$ (KNLF)	A. Lempicki* B. McCollum* S. R. Chinn	Accepted by IEEE J. Quantum Electron.
4966	Ionization Coefficients of Electrons and Holes in InP	C. A. Armiento S. H. Groves C. E. Hurwitz	Accepted by Appl. Phys. Lett.
4978	Subtraction of Signal Overlaps in Rutherford Backscattering Spectrometry	Z. L. Liao	Accepted by Appl. Phys. Lett.
4981	A SAW/CCD Programmable Matched Filter	R. W. Ralston D. L. Smythe E. Stern	Accepted by Appl. Phys. Lett.
4989	A New Cut of Quartz for Temperature-Stable SAW Dispersive Delay Lines	D. E. Oates	Accepted by IEEE Trans. Sonics Ultrason.
5000	Replication of 175 Å Lines and Spaces in PMMA by X-Ray Lithography	D. C. Flanders	Accepted by Appl. Phys. Lett.
5005	Directional Oxygen-Ion-Beam Etching of Carbonaceous Materials	P. D. DeGraff D. C. Flanders	Accepted by J. Vac. Sci. Technol.
5006	X-Ray Lithography at ~100 Å Linewidths Using X-Ray Masks Fabricated by Shadowing Techniques	D. C. Flanders	
5007	Spatial-Period-Division - A New Technique for Exposing Submicrometer-Linewidth Periodic and Quasi-Periodic Patterns	D. C. Flanders A. M. Hawryluk H. I. Smith	
5008	Graphoepitaxy of Silicon on Fused Silica Using Surface Micropatterns and Laser Crystallization	M. W. Geis D. C. Flanders H. I. Smith D. A. Antoniadis*	
5009	X-Ray Zone Plates Fabricated Using Electron Beam X-Ray Lithography	D. C. Shaver D. C. Flanders N. M. Ceglio* H. I. Smith	

Meeting Speeches†

MS No.			
4177G	Sputtered Films for Wavelength-Selective Applications	J. C. C. Fan	1979 Spring Mtg. of American Vacuum Society, Rochester, New York. 19 June 1979

*Author not at Lincoln Laboratory.

†Titles of Meeting Speeches are listed for information only. No copies are available for distribution.

MS No.

4802C	Vibrational Kinetics in Cryogenic Liquids and Applications to Nonlinear Optics	S. R. J. Brueck T. F. Deutsch H. Kildal R. M. Osgood, Jr.	NATO Advanced Study Institute, Menton, France, 25 June - 7 July 1979
4863	Molecular-Beam Epitaxy of IV-VI Semiconductors on IV-VI Substrates	J. N. Walpole	Molecular Beam Epitaxy Symp., Boston, 6-11 May 1979
4876	FM Mode-Locked $\text{Nd}_{0.5}\text{La}_{0.5}\text{P}_5\text{O}_{14}$ Laser	S. R. Chinn W. K. Zwickler*	
4904	Laser Initiated Deposition of Metal Films with Microscopic Dimensions	T. F. Deutsch D. J. Ehrlich R. M. Osgood, Jr.	
4905	Optically Pumped Photodissociation Lasers	D. J. Ehrlich R. M. Osgood, Jr.	
4907	Submillimeter Double Resonance Study of CH_3F Using Reradiation from Schottky Barrier Diodes	W. A. M. Blumberg H. R. Fetterman D. D. Peck P. F. Goldsmith*	
4908	Third Harmonic Generation and Infrared Kerr Switching in Cryogenic Liquids - Efficiency Limitations and Applications	H. Kildal S. R. J. Brueck	CLEA '79, Washington, D. C., 30 May - 1 June 1979
4911	Frequency and Spatial Hole-Burning Properties of $\text{Ga}_x\text{Al}_{1-x}\text{As}$ External-Cavity Diode Lasers	M. W. Fleming A. Mooradian	
4912	Continuously Tunable cw Ni:MgF_2 Laser	P. F. Moulton A. Mooradian	
5033	UV Solid-State Ce:YLF Laser at 325.5 nm	D. J. Ehrlich P. F. Moulton R. M. Osgood, Jr.	
5047	Efficient Infrared ac Kerr Switches Using Simple Cryogenic Liquids	S. R. J. Brueck H. Kildal	
4878B	Liquid-Phase Epitaxy of $\text{Hg}_{1-x}\text{Cd}_x\text{Te}$	T. C. Harman	
4904A	Laser Photodeposition of Films with Micrometer Size Features	D. J. Ehrlich T. F. Deutsch R. M. Osgood, Jr.	21st Electronic Materials Conf., University of Colorado, Boulder, 27-29 June 1979

* Author not at Lincoln Laboratory.

MS No.			
4988	Growth Rates, Morphology, and Doping of CVD GaAs Epilayers on Polycrystalline GaAs Substrates	R. P. Gale F. M. Davis J. C. C. Fan C. O. Bozler	21st Electronic Materials Conf., University of Colorado, Boulder, 27-29 June 1979
4995	Laser Crystallization of Thin Amorphous Germanium Films	J. C. C. Fan R. L. Chapman R. P. Gale H. J. Zeiger	
4883C	Solar Photovoltaic Cells	J. C. C. Fan	New England Chapter of American Chemical Society, Woburn, Massachusetts, 21 June 1979
4905B	Stimulated Optical Phenomena in Photodissociation Lasers	D. J. Ehrlich R. M. Osgood, Jr.	1979 Gordon Research Conference, Wolfeboro, New Hampshire, 2-6 July 1979
5047A	Third-Order Nonlinear Coefficients of Cryogenic Liquids	H. Kildal S. R. J. Brueck	
4949	Effect of Pressure and Composition on Fast Na ⁺ -Ion Transport in the System Na _{1+x} Zr ₂ Si _x P _{3-x} O ₁₂	J. A. Kafalas R. J. Cava*	Intl. Conf. on Fast Ion Transport in Solids, Lake Geneva, Wisconsin, 21-25 May 1979
4986	Crystal Structure and Ionic Conductivity of a New Superionic Conductor, Na ₃ Sc ₂ P ₃ O ₁₂	H. Y-P. Hong	
4996	Analysis of the Alternating Current Properties of LISICON Ceramics	M. L. Bayard	
4952	Ion-Implanted, Laser-Annealed GaAs Solar Cells	J. C. C. Fan R. L. Chapman J. P. Donnelly G. W. Turner C. O. Bozler	37th Annual Device Research Conf., University of Colorado, Boulder, 25-27 June 1979
4960	High-Speed InP Optoelectronic Switch	F. J. Leonberger P. F. Moulton	
4993	Ionization Coefficients of Electrons and Holes in InP	C. A. Armiento S. H. Groves C. E. Hurwitz	
4994	Guarded Avalanche Photodiodes in InP Fabricated by a Double Ion Implantation Technique	J. P. Donnelly V. Diadiuk C. A. Armiento S. H. Groves G. W. Iseler	
5044	1.0-1.6 μm Sources and Detectors for Fiber Optics Applications	A. G. Foyt	

*Author not at Lincoln Laboratory.

MS No.			
4959	Surface-Acoustic-Wave Convolvers for Processing Spread-Spectrum Signals	R. C. Williamson	Natl. Radio Science Mtg., University of Washington, Seattle, 18-22 June 1979
4965	Doppler-Limited Spectroscopy of the $3\nu_3$ Band of SF_6	A. S. Pine	34th Annual Symp. on Molecular Spectroscopy, Ohio State University, 11-15 June 1979
5055	Deconvolving Infrared Spectra Beyond the Doppler Limit	J. Pliva* A. S. Pine	
4966	Spatial Period Division - A New Technique for Fabricating Gratings	D. C. Flanders A. M. Hawryluk H. I. Smith	
4967	Micromorphotaxy of Silicon on Fused Silica Using Surface Micropatterns and Laser Crystallization	M. W. Geis D. C. Flanders H. I. Smith	Electron, Ion and Photon Beam Technology Symp., Boston, 29 May - 1 June 1979
4968	X-ray Zone Plates Fabricated Using Electron-Beam and X-ray Lithography	D. C. Shaver D. C. Flanders N. M. Ceglio* H. I. Smith	
4976	X-ray Lithography at $\sim 100 \text{ \AA}$ Linewidths Using X-ray Masks Fabricated by Shadowing Techniques	D. C. Flanders	
5043	Directional Oxygen-Ion-Beam Etching of Carbonaceous Materials	P. D. DeGraff D. C. Flanders	
4974	Infrared Electroluminescence as a Diagnostic Tool for Polycrystalline GaAs Solar Cells	G. W. Turner J. C. C. Fan J. P. Salerno	Photovoltaic Material and Device Measurements Workshop, Arlington, Virginia, 11-13 June 1979
5013	Four-Wave Interactions in Acoustoelectric Integrating Correlators	R. W. Ralston	Boston Section IEEE, Raytheon Co., Bedford, Massachusetts, 23 May 1979
5023	Excited State Spectroscopy and Kinetics of CH_3F Using Tunable Submillimeter Sources	W. A. M. Blumberg H. R. Fetterman D. D. Peck P. E. Tannenwald	Microwave Spectroscopy and Coherent Radiation Symp., Duke University, Durham, No. Carolina, 18-20 June 1979
5024	Tunable Diode Lasers and Their Spectroscopic Applications	A. Mooradian	Vavilov Conference on Lasers, Novosibirsk, USSR, 20-23 June 1970
5027	Shallow-Homojunction GaAs Solar Cells	J. C. C. Fan	3rd High Efficiency Solar Cell Mtg., Cleveland, Ohio, 13-14 June 1979

* Author not at Lincoln Laboratory.

<u>MS No.</u>			
5028	Tunable Transition-Metal Doped Solid State Lasers	P. F. Moulton A. Mooradian	} 4th Intl. Conf. on Laser Spectroscopy, Tegernsee, Germany, 11-15 June 1979
5029	Metal-Atom Photodissociation Lasers	D. J. Ehrlich R. M. Osgood, Jr.	
5032	Development and Preliminary Operation of a 5 and 10 μm DIAL System	P. L. Kelley D. Killinger N. Menyuk A. Mooradian P. F. Moulton W. E. DeFeo	9th Intl. Laser Radar Conf. on Laser Atmospheric Studies, Munich, Germany, 2-5 July 1979
5038	Electrooptical Device Development at Lincoln Laboratory	A. G. Foyt	Seminar, Aerospace Corp., Los Angeles, 9 May 1979
5048	The Interaction of CO with ZnO	R. R. Gay E. I. Solomon* V. E. Henrich* H. J. Zeiger	39th Physical Electronics Conf., University of Maryland, College Park, 18-20 June 1979
5050	Comparison of Surface-Acoustic-Wave and Optical Signal Processing	R. C. Williamson	SPIE Electro-Optical Technical Symp. and Workshop, Huntsville, Alabama, 22-25 May 1979
5084	Surface-Wave Devices for Analog Signal Processing	S. A. Reible R. C. Williamson	Seminar, University of Wisconsin, 28 June 1979
5089	Reliability and Performance of Long Wavelength, Quaternary-Based Lasers	J. N. Walpole	Gordon Research Conference on Point and Line Defects in Semiconductors, Kimball Union Academy, Meriden, New Hampshire, 25 July 1979

*Author not at Lincoln Laboratory.

ORGANIZATION

SOLID STATE DIVISION

A.L. McWhorter, *Head*
I. Melngailis, *Associate Head*
J.F. Goodwin, *Assistant*
P.E. Tannenwald, *Senior Staff*

QUANTUM ELECTRONICS

A. Mooradian, *Leader*
P.L. Kelley, *Associate Leader*

Barch, W.E.	Fleming, M. W.*
Belanger, L.J.	Hancock, R. C.
Blumberg, W.A.M.	Kildal, H.
Brueck, S.R.J.	Killinger, D. K.
Burke, J.W.	Menyuk, N.
Chinn, S.R.	Moulton, P. F.
DeFeo, W.E.	Osgood, R. M., Jr.
Deutsch, T.F.	Parker, C. D.
Ehrlich, D.J.	Peck, D. D.
Feldman, B.	Pine, A. S.
Fetterman, H.R.	

ELECTRONIC MATERIALS

A.J. Strauss, *Leader*
H.J. Zeiger, *Associate Leader*
J.G. Mavroides, *Senior Staff*

Anderson, C. H., Jr.	Hsieh, J. J.
Button, M. J.	Iseler, G. W.
Chapman, R. L.	Kafalas, J. A.
Davis, F. M.	Kolesar, D. E.
Delaney, E. J.	Krohn, L., Jr.
Fahey, R. E.	Mastromattei, E. L.
Fan, J. C. C.	Owens, E. B.
Finn, M. C.	Palm, B. J.
Flutie, R. E.	Pantano, J. V.
Foley, G. H.	Salerno, J. P.*
Gale, R. P.	Tracy, D. M.
Gay, R. R.*	Vohl, P.
Hong, H. Y-P.	

APPLIED PHYSICS

A.G. Foyt, *Leader*
C.E. Hurwitz, *Associate Leader*
T.C. Harman, *Senior Staff*
R.H. Kingston, *Senior Staff*

Armiento, C. A.*	Leonberger, F. J.
Calawa, A. R.	Liau, Z-L.
Carter, F. B.	Lind, T. A.
DeMeo, N. L., Jr.	McBride, W. F.
Diadiuk, V.	Paladino, A. E.
Donnelly, J. P.	Plonko, M. C.
Duffy, P. E.	Spears, D. L.
Ferrante, G. A.	Tsang, D. Z.*
Glasser, L. A.*	Walpole, J. N.
Groves, S. H.	

ANALOG DEVICE TECHNOLOGY

E. Stern, *Leader*
R.C. Williamson, *Associate Leader*

Anderson, A. C.	Hurlburt, D. H.
Arsenault, D. R.	Kernan, W. C.
Baker, R. P.	Oates, D. E.
Becker, R. A.	Ralston, R. W.
Brogan, W. T.	Reible, S. A.
Cafarella, J. H.	Slattery, R. L.
DiPerna, M. S.	Withers, R. S.
Dolat, V. S.	Yao, I.
Holtham, J. H.	

MICROELECTRONICS

W.T. Lindley, *Leader*
F.J. Bachner, *Associate Leader*
H.I. Smith, *Assistant Leader*

Alley, G. D.	Gray, R. V.
Baker, E. M.	Hansell, G. L.*
Bozler, C. O.	Hawryluk, A. M.*
Burke, B. E.	Jacobsen, E. H.
Chiang, A. M.	Lincoln, G. A., Jr.
Chu, A.	McGonagle, W. H.
Clifton, B. J.	Melngailis, J.
Daniels, P. J.	Mountain, R. W.
DeGraff, P. D.	Murphy, R. A.
Durant, G. L.	Pichler, H. H.
Eastman, I. F.	Shaver, D. C.*
Efremow, N., Jr.	Silversmith, D. J.
Elta, M. E.	Smythe, D. I., Jr.
Felton, B. J.	Sotomayer-Diaz, O.*
Flanders, D. C.	Turner, G. W.
Geis, M. W.	Wilde, R. E.
Gopinath, A.	

* Research assistant

I. SOLID STATE DEVICE RESEARCH

A. FABRICATION OF OHMIC CONTACTS ON p-InP USING ION IMPLANTATION AND LASER ANNEALING

Low-resistance ohmic contacts are important for many semiconductor devices, including diode lasers, where minimum heating is required for high efficiency and reliability. Difficulties have been experienced in conventional Au-Zn alloy contacts on p-InP, because the Au-Zn evaporation and alloying processes are not easily controllable and often nonreproducible. Recently, laser-annealing techniques have demonstrated the capability of obtaining good ohmic contacts on GaAs (see Refs. 1 to 4). Here we report the first study of this kind on InP. Our approach is to use ion implantation and Q-switched laser annealing to produce an extremely heavily doped surface layer, on which evaporated Au, without microalloying, can be used for a good ohmic contact.¹

The InP substrates used in these experiments were pulled (100)-oriented p-type samples with a hole concentration of $1.25 \times 10^{18} \text{ cm}^{-3}$. After polishing and etching, the samples were implanted with $(0.5 \text{ to } 7) \times 10^{15} \text{ cm}^{-2}$ of 30-keV Zn^+ or Cd^+ ions. The implantations were carried out at room temperature with substrates tilted 7° away from the normal ion incidence. The implanted sample was then mounted on a micromanipulator for laser annealing. In these experiments we have investigated two different lasers, a Q-switched Nd:YAG laser operating at $1.06 \mu\text{m}$ and a Q-switched ruby laser operating at $0.694 \mu\text{m}$. Best results to date have been obtained using the Nd:YAG laser; therefore, this report will deal primarily with these Nd:YAG results and only briefly mention the ruby laser for comparison purposes.

The Nd:YAG laser beam ($\lambda = 1.06 \mu\text{m}$) was focused to a spot of $\sim 100 \mu\text{m}$ diameter on the sample. The laser was operated in an acoustooptically Q-switched mode with a pulse duration of 250 nsec and a repetition rate of 20 Hz. The peak power of a pulse was determined to be $1.5 \times 10^3 \text{ W}$. By varying the sample position (both parallel and perpendicular to the beam), arrays of isolated spots irradiated at various effective power densities were obtained on one sample. Arrays of Au dots, each covering one annealed spot, were then made by photolithography and Au evaporation.

Figure I-1(a-f) shows optical micrographs of several annealed spots on a sample implanted with $3 \times 10^{15} \text{ cm}^{-2} \text{ Zn}^+$. The micrographs correspond to a sequence of results obtained on one sample which was translated and moved away from the laser focal point by equal steps. For the higher power densities [Figs. I-1(a) through (c)], irradiated spots show evidence of melting and a high vapor pressure during the laser pulse irradiation. For lower power densities [Figs. I-1(d) through (f)], the spots are flat except for the boundaries which presumably separated the melted and unmelted regions during the annealing process. The I-V measurement between each spot of Fig. I-1(a-f) and another one that was irradiated at identical power density (on the same sample) showed ohmic characteristics. Figures I-2(a) through (c) correspond to Figs. I-1(d) through (f), while Fig. I-2(d) shows the I-V characteristic of Au dots on an unannealed area.

Experiments with misaligned Au dots showed that, in an irradiated spot, the region effective for ohmic contacts was within the visible morphological changes. Thus the average specific contact resistance within the spots of Figs. I-1(d) through (f) are determined to be 2.2×10^{-4} , 1.3×10^{-4} , and $5 \times 10^{-5} \Omega\text{-cm}^2$, respectively, while that of the conventional Au-Zn alloy contact made on the same (but unimplanted) InP substrate was $3 \times 10^{-4} \Omega\text{-cm}^2$.

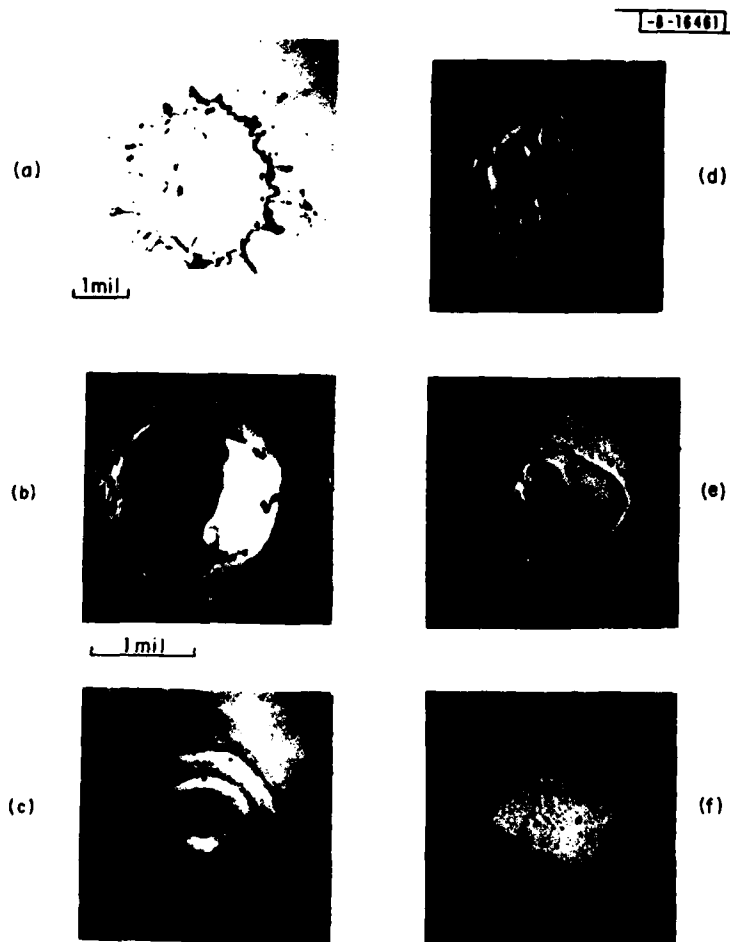


Fig.1-1(a-f). Laser-annealed spots with sample moved away from focal point by equal steps. Each spot has been coated by a 5×5 -mil Au dot after laser annealing.

-8-16462

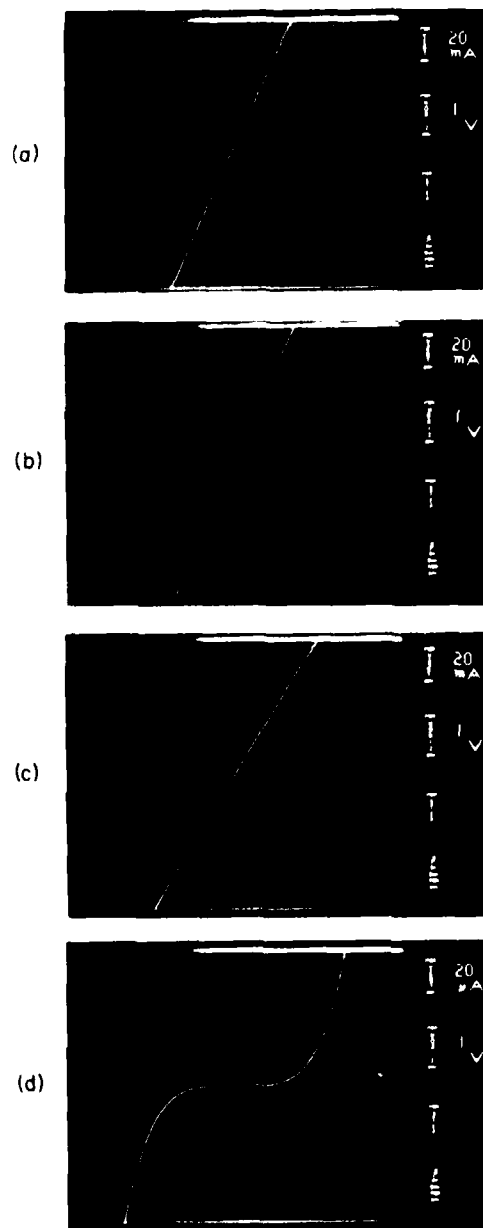


Fig.1-2. I-V characteristics of Au contacts on laser-annealed spots [(a) through (c)] and unannealed area (d).

Experiments with Cd^+ -implanted samples showed that a dose of $1 \times 10^{15} \text{ cm}^{-2}$ resulted in highly resistive and non-ohmic contacts. With a Cd^+ dose of $3 \times 10^{15} \text{ cm}^{-2}$, ohmic characteristics with the resistance nearly a factor-of-2 higher than that of Zn^+ samples was obtained. Only ~30-percent improvement was achieved by increasing the Cd^+ dose to $7 \times 10^{15} \text{ cm}^{-2}$. So far, the lowest resistance [~40-percent lower than that of Fig.1-2(b)] was obtained by using a sample with dual implants ($3 \times 10^{15} \text{ cm}^{-2} \text{ Zn}^+$ and $1 \times 10^{15} \text{ cm}^{-2} \text{ Cd}^+$).

With Q-switched ruby-laser ($\lambda = 0.694 \mu\text{m}$, pulse duration $\approx 50 \text{ nsec}$) annealing, the best results were obtained on a Zn^+ -implanted sample annealed at a power density $\sim 10 \text{ MW/cm}^2$. However, the specific contact resistance was $\sim 2 \times 10^{-2} \Omega\text{-cm}^2$, which was 10^2 times higher than that obtained by using the Nd:YAG laser.

The present results can be explained in terms of transient melting and regrowth, which repairs the implantation damage and activates the implanted dopants to exceedingly high concentrations. Because it is necessary to melt to the depth of the implantation damage distribution, a higher power density will be required to anneal samples of higher-energy implant. This high power density can also promote the evaporation of the sample material. The resulting high vapor pressure is likely to be responsible for the apparent surface "damage" such as that seen in Figs.1-1(a) through (c). Since only a thin ($\leq 200\text{-}\text{\AA}$) surface layer of heavy doping is required for a good ohmic contact, it is desirable to use as low an implantation energy as possible and to use a laser power density just high enough to melt to the implantation depth.

The rather different results obtained by the ruby-laser annealing can possibly be explained by the fact that, to melt to the same depth, the ruby laser will produce a higher transient surface temperature because of its shorter pulse duration and shorter wavelength. We suggest that temperatures higher than the melting point are not only unnecessary, but also undesirable, since they can result in excess dissociation and/or evaporation of the acceptors. In combination with the liquid-state diffusion, this can possibly result in a depletion or compensation of the acceptors in the first few hundred angstroms, which is of vital importance to ohmic contacts.

In conclusion, we have shown that good ohmic contacts on p-InP, with a specific contact resistance lower than that obtained by conventional alloying techniques, can be obtained by using a combination of ion implantation and pulsed laser annealing. To achieve a low resistance and avoid surface damage, it is necessary to use low ion-implantation energies and laser pulses with a suitable power density and pulse duration to achieve melting to the implantation depth without heating the surface to a temperature significantly higher than the melting point.

Z-L. Liao	D. E. Mull
N. L. DeMeo, Jr.	R. Bradbury†
J. P. Donnelly	J. P. Lorenzo†

B. Ti-DIFFUSED OPTICAL WAVEGUIDE DEVICES IN LiNbO_3

An analysis of performance considerations for a high-speed guided-wave electrooptic A/D converter was presented in a previous report.⁵ Based on that analysis, it was concluded that the development of converters with 4- to 6-bit accuracy at a 1-GS/sec conversion rate should be feasible. As a preliminary step in converter development, Ti-diffused waveguide devices in LiNbO_3 have been successfully fabricated and tested. Results are reported here on directional couplers and branching waveguides as well as on single-mode electrooptic interferometer modulators characterized by a 17-dB extinction ratio.

† Rome Air Development Center, Griffiss Air Force Base, New York.

Three-dimensional waveguides were formed on X-cut crystals by using sputtered Ti and conventional photolithographic, chemical etching, and diffusion techniques.⁶ The waveguides were approximately 3 μm thick and were oriented in the Y crystallographic direction. Li_2O outdiffusion during the Ti diffusion was minimized using previously reported techniques.⁷ (The Li_2O outdiffusion forms a slab waveguide for TE modes but has no effect on TM modes, and must be compensated for in converter design because use of the TE polarization requires a drive power a factor-of-10 less than that required for TM polarization.) Following the diffusion, the end faces of the crystal were polished so that waveguide testing could be done using end-fire coupling. This end-face polishing required a special technique to obtain the desired square, chip-free edge at the top surface of the crystal.

Figure I-3(a-b) shows results for typical branching waveguides and directional couplers we have fabricated. To the left is a sketch indicating the branching Y and directional couplers that are shown in the photomicrographs. The waveguides are visible in the photos because of the slight surface swelling that occurs during the diffusion. The waveguides are on the order of $10 \times 3 \mu\text{m}$ and the fundamental mode has been excited. The photographs to the right indicate the clean outputs obtained for TE-polarized light from a He:Ne laser at 0.63 μm . These photos were obtained by imaging the waveguide output face on a vidicon and photographing the resulting image displayed on a television monitor. The lack of scattered light in the branching Y between the guides should be noted. The directional coupler is functioning as an $\sim 3\text{-dB}$ coupler.

Single-mode electrooptic interferometric modulators, which are the fundamental components of the A/D converter, have also been successfully fabricated and tested. These devices had 3- μm -wide guides, a total branching angle at each Y of 2° , an electrode length of 3 mm, and a spacing of 25 μm between modulator arms (see inset in Fig.I-4). A typical plot of modulator output intensity vs applied voltage for a TE-polarized input at $\lambda = 0.63 \mu\text{m}$ is shown in Fig.I-4. For these data, the center electrode and one of the outer electrodes were grounded and bias was applied to the other outer electrode. The data were obtained using end-fire coupling and by forming a magnified image of the near-field pattern of the modulator output face on an apertured photodiode that was operated in a synchronous detection mode.⁸ As shown in the figure, 4.4 V is required to obtain a π -phase shift, which is consistent with calculated values. An extinction ratio of 17 dB (98 percent) has been obtained. The achievement of multiple 17-dB minima with increasing bias represents better performance for this type of modulator than has previously been reported. The modulators have also been driven by a 30-V triangular waveform to obtain modulation at $\sim 130 \text{ kHz}$ of the 0.63- μm light. From examining the output from single guides and Y branches fabricated on the same wafer with the modulators, it is estimated that the modulator insertion loss is only $\sim 1\text{-dB}$ greater than a straight guide and that the power division at a Y is within $\leq 0.2 \text{ dB}$ of 50 percent. The deviation from maximum output at zero bias for the device shown indicates an arm-length difference of $\sim 0.1 \mu\text{m}$; other devices have exhibited nearly peak output at zero bias.

F.J. Leonberger
F.J. O'Donnell

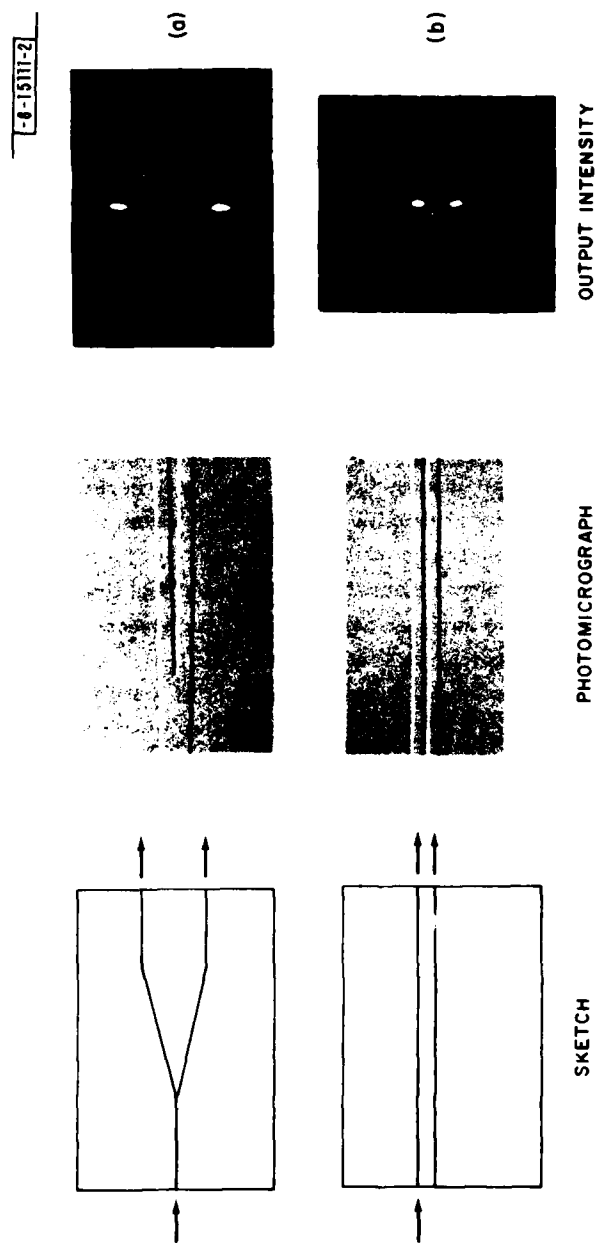


Fig.1-3. Sketches, photomicrographs, and near-field output intensity photographs for (a) branching waveguides and (b) directional couplers formed by Ti diffusion into LiNbO_3 .

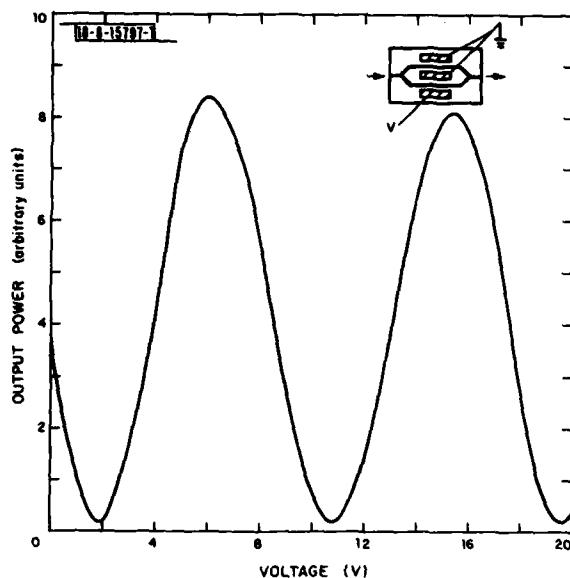


Fig. I-4. Output intensity vs bias for Ti-diffused LiNbO_3 single-mode electrooptic interferometric modulator.

REFERENCES

1. P.A. Barnes, H.J. Leamy, J.M. Poate, S.D. Ferris, J.S. Williams, and G.K. Celler, *Appl. Phys. Lett.* **33**, 965 (1978).
2. S. Margalit, D. Fekete, D.M. Pepper, C.P. Lee, and A. Yariv, *Appl. Phys. Lett.* **33**, 346 (1978).
3. R.B. Gold, R.A. Powell, and J.F. Gibbons, in *Laser-Solid Interactions and Laser Processing - 1978*, S.D. Ferris, H.J. Leamy, and J.M. Poate, Eds. (American Institute of Physics, New York, 1979), p.635.
4. G. Eckhardt, C.L. Anderson, L.D. Hess, and C.F. Krumm, *Ibid.*, p.641.
5. Solid State Research Report, Lincoln Laboratory, M.I.T. (1979:2), pp.9-14.
6. R.V. Schmidt and I.P. Kaminow, *Appl. Phys. Lett.* **25**, 458 (1974).
7. B. Chen and A.C. Pastor, *Appl. Phys. Lett.* **30**, 770 (1977).
8. F.J. Leonberger, J.P. Donnelly, and C.O. Bozler, *Appl. Phys. Lett.* **29**, 652 (1976), DDC AD-A037627/7.

II. QUANTUM ELECTRONICS

A. DIFFERENTIAL-ABSORPTION MEASUREMENTS OF ATMOSPHERIC CO USING A FREQUENCY-DOUBLED CO₂ LIDAR SYSTEM

Single-ended laser remote sensing measurements have been made of the atmospheric concentration of CO using a differential-absorption, frequency-doubled CO₂ LIDAR system. A schematic of the experimental apparatus used in these experiments is shown in Fig. II-1. A mini-TEA CO₂ laser was used to generate line-tunable, pulsed radiation near 9.3 μm at a repetition rate of 25 Hz. The frequency of the CO₂ laser was monitored through use of a spectrometer to ensure single-frequency operation. The laser radiation was frequency doubled through use of a CdGeAs₂ crystal. The generated radiation near 4.65 μm had a pulse length of 70 nsec, an energy per pulse of 0.2 mJ, and a beam divergence of approximately 2 mrad. The linewidth of the 4.65- μm radiation was approximately 0.02 cm^{-1} .

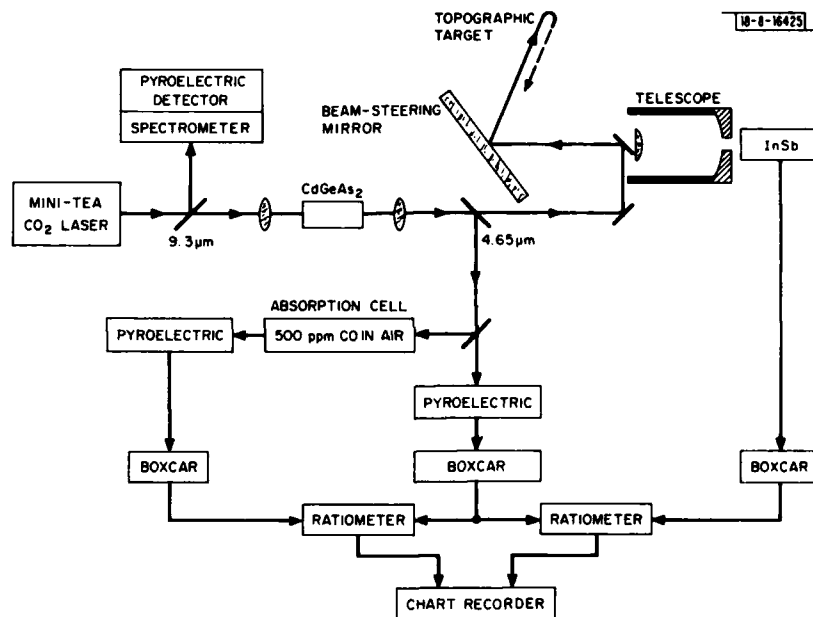


Fig. II-1. Schematic of experimental apparatus for laser remote sensing measurements.

A laser-power normalization signal and an absorption calibration for the doubled laser frequencies were obtained by splitting off portions of the 4.65- μm radiation. The remainder of the 4.65- μm laser beam was directed by a 50-cm beam-steering mirror toward topographic targets located outside a laboratory window. Pulsed laser radiation backscattered from the target was collected by a collinear 30-cm Cassegrainian telescope and detected with an InSb detector located at the focal plane of the collection optics. The output signal from the InSb detector was processed through a 1- μsec gated boxcar integrator and normalized to the laser power through use of the reference pyroelectric detector output.

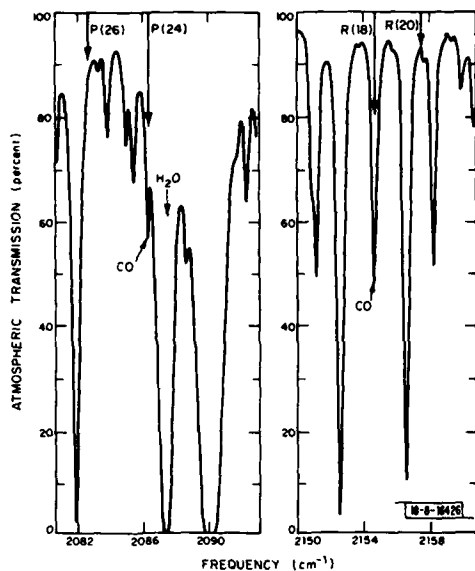


Fig. II-2. Synthetic transmission spectrum of atmosphere (3-km path length, 29-percent relative humidity) and spectral position of doubled CO₂-laser frequencies useful for CO detection.

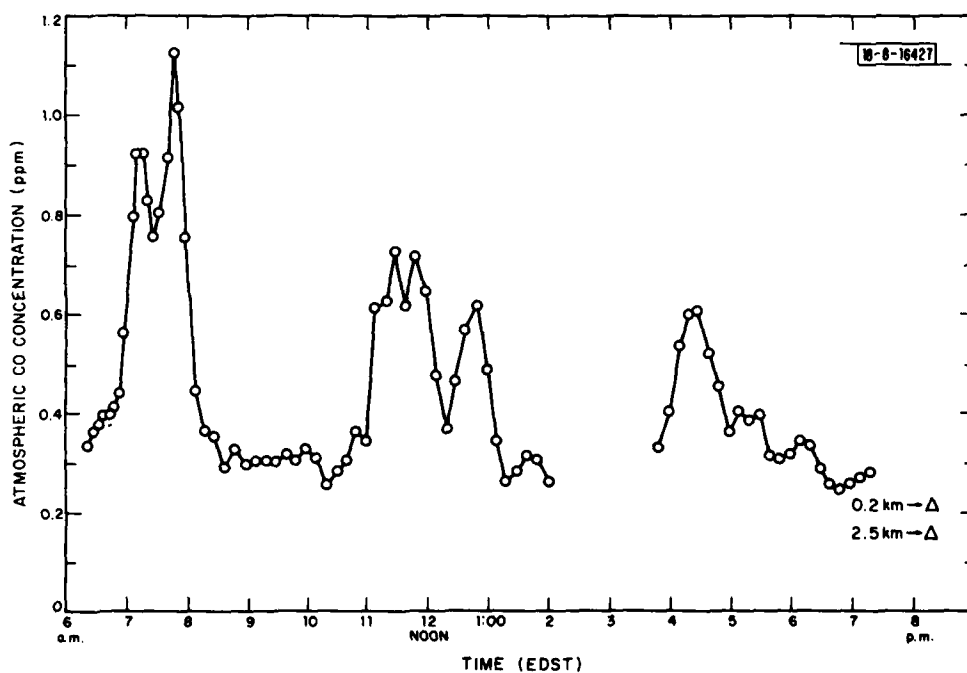


Fig. II-3. Measured diurnal variation of average atmospheric CO concentration over 13-hr span on 6 July 1979 for path length of 0.5 km which traversed major traffic roadway located at 0.48 km distance.

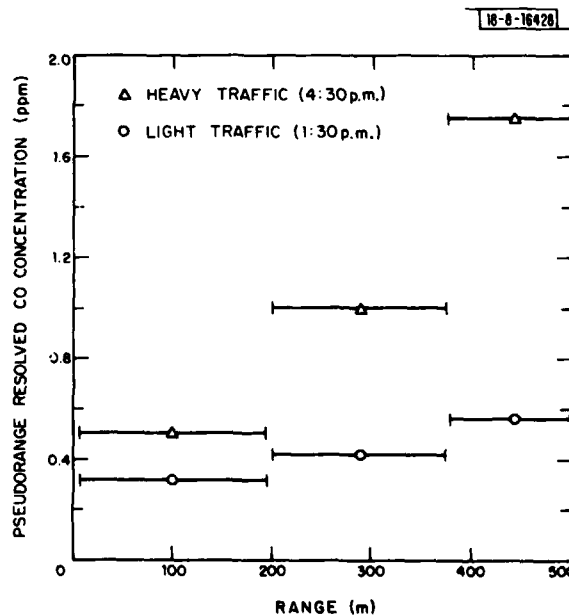
The concentration of CO is deduced from differences in the normalized laser return as the laser frequency is tuned through those CO₂-laser frequencies which, when doubled, are absorbed by CO.

For detection of CO using frequency-doubled radiation from our mini-TEA CO₂ laser, two absorption coincidences may be utilized - the doubled R(18) line of CO₂ with the R(2) transition of CO near 2154.59 cm⁻¹, and the doubled P(24) line of CO₂ with the P(14) line of CO near 2086.32 cm⁻¹. The R(18) absorption coincidence is relatively free of interference from nearby absorption lines due to other atmospheric gases, while the P(24) line requires only slight correction due to the presence of water vapor. This may be seen in Fig. II-2 where the synthetic transmission spectrum of the atmosphere is shown along with the absorption coincidences and off-resonance lines of the doubled CO₂-laser radiation. The average concentration of CO (integrated over the path of the laser beam) is deduced from a comparison of the on-resonance to off-resonance detected laser backscatter ratio with that obtained simultaneously from the laboratory absorption cell.

Figure II-3 shows the atmospheric concentration of CO measured over a 13-hr period for a path which traversed a main traffic roadway located 0.48 km from Lincoln Laboratory. The topographic target used was a painted sign located approximately 0.02 km on the far side of the traffic roadway. These results were obtained using the R(18) absorption coincidence; results obtained using the P(24) coincidence agreed within 15 percent. The diurnal variation of CO shown in Fig. II-3 was obtained by smoothing the collected data over 15-min. intervals, and clearly reflects the increased vehicular traffic during the periods of morning arrival, lunchtime, and evening departure of a working day. The actual time resolution was on the order of a few seconds, which permitted the observation of individual cars and trucks as they passed along the roadway. Also shown in Fig. II-3 is the average CO concentration measured at 8:00 p.m. using the reflected laser return from a 1-in.-diam retroreflector located 2.5 km away, and from a telephone pole 200 m distant which did not encompass any major traffic roadways.

Pseudorange resolution measurements were obtained by utilizing several targets at different ranges along the same line-of-sight. By differentiating the integrated path measurements obtained for different ranges, the strong localization of the CO concentration over the traffic roadway was clearly established. Our results are shown in Fig. II-4 where the CO concentration was

Fig. II-4. Pseudorange resolved measurements of atmospheric CO deduced from differentiation of integrated path measurements obtained on 22 June 1979 from laser return from targets at 200, 375, and 500 m along same line-of-sight. Path for farthest target at 500 m encompassed traffic roadway located at 0.48 km.



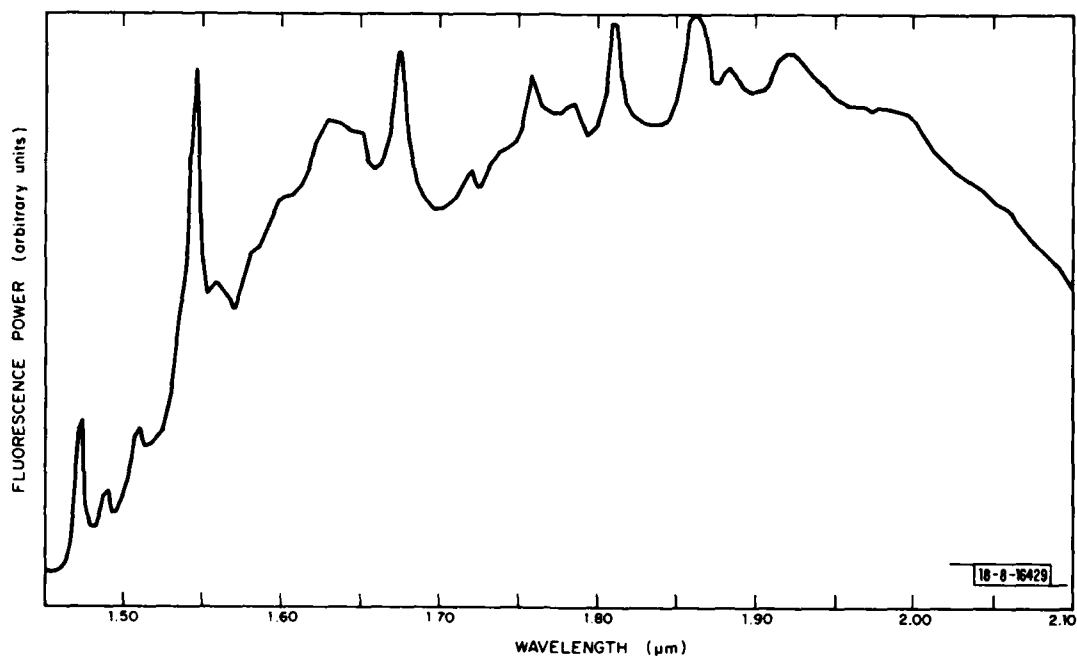


Fig. II-5. Fluorescence spectrum at 77 K from Co:MgF₂.

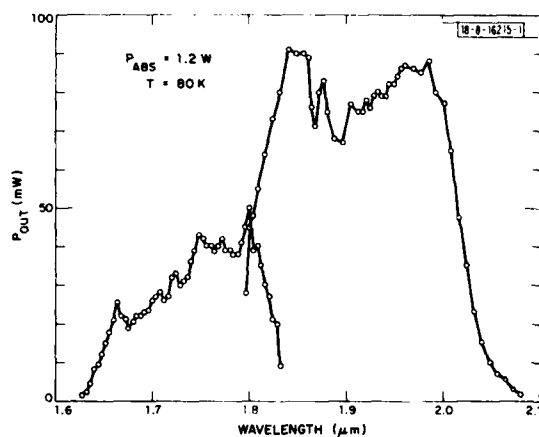


Fig. II-6. Tuning curves from Co:MgF₂ laser. Two sets of mirrors were required to tune over entire range, hence two curves.

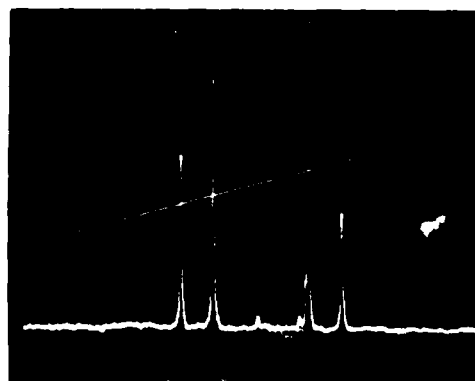


Fig. II-7. Longitudinal mode spectrum of Ni:MgF₂ from scanning confocal interferometer. Total frequency scanned by ramp voltage shown in picture is 3.75 GHz.

measured at ranges of 200, 375, and 500 m at two different times – one when the traffic was relatively heavy on the roadway encompassed only by the 500-m range path and the other when it was relatively light. It should be noted that the time variation of the detected signal for the on-resonance R(18) line showed large changes (factors of 5 or more) in the CO concentration due to individual cars and trucks. No such effect was observed for the off-resonance R(20) return. In addition, only small (± 5 percent) short-term variations in the detected backscatter were observed for either the R(18) line or the R(20) line for the long-path (~ 2.5 -km) measurement reported in Fig. II-3. This indicates that the effect of atmospheric turbulence on the propagation characteristics of the laser beam were negligible under the conditions of our experiments, and that our present system is capable of providing a measure of the instantaneous CO concentration under conditions of heavy vehicular traffic.

D. K. Killinger
N. Menyuk
W. E. DeFeo

B. ADVANCES IN TRANSITION-METAL-DOPED LASERS

The first CW operation of a Co:MgF₂ laser has been obtained. The laser exhibits continuous tuning over a 1300-cm^{-1} range from 1.63 to $2.08\text{ }\mu\text{m}$ in a three-mirror-cavity, Nd:YAG laser-pumped arrangement described previously.¹ The fluorescence spectrum for the $^4T_2 - ^4T_1$ laser transition of Co⁺² in MgF₂ at 77 K is shown in Fig. II-5. The Co⁺² ground state is split into six levels having energies of 152, 798, 1087, 1256, and 1396 cm^{-1} above the lowest-lying level.² The fluorescence shown is a mixture of purely electronic and vibronic transitions. The peak around $1.54\text{ }\mu\text{m}$ is due to a small quantity of Ni⁺² impurities in the sample, efficiently excited³ by radiationless transfer from Co⁺². The tuning curves for the Co:MgF₂ laser at a crystal temperature of 80 K are shown in Fig. II-6. Two sets of mirrors were required to obtain operation over the tuning range. The 0.2-percent-transmission output coupler used to generate the short-wavelength curve was less optimal than the 0.5-percent-transmission mirror used for the long-wavelength curve, hence the difference in average output power levels between the two curves. At 1.4 W of absorbed $1.33\text{-}\mu\text{m}$ pump power, operation with a 0.5-percent coupler was at 3.7 times threshold for a $1.97\text{-}\mu\text{m}$ operating wavelength.

The longitudinal mode properties of a three-mirror-cavity Ni:MgF₂ laser¹ have been examined using a scanning confocal interferometer. With a birefringent tuning element in the cavity, laser operation was primarily in 3 to 4 longitudinal modes contained within a 1.5-GHz-frequency region. A typical mode pattern is shown in Fig. II-7. Two pairs of modes are observed, with the spacing between the two modes in each pair equal to the full cavity mode spacing of 260 MHz, and the spacing between the two pairs equal to about 1 GHz. Spatial hole-burning theory⁴⁻⁶ predicts in the limit of an infinitely short active medium that only two modes spaced by $c/4l'$ will oscillate, where l' is the spacing between the active medium and the nearest cavity mirror. For the Ni:MgF₂ laser cavity, $c/4l'$ is 1 GHz – the spacing between the two pairs of observed modes. The observation of four rather than two modes may be the result of the finite length of the laser crystal.

Single-frequency operation of the Ni:MgF₂ laser with an output power of 20 mW was obtained using two tilted intracavity fused-silica etalons with thicknesses of 0.28 and 0.95 cm. In a single scan of the interferometer the observed laser linewidth was 20 MHz, which was most likely the finesse-limited linewidth of the interferometer. The frequency stability of the laser over a 0.5-sec measurement period was ± 35 MHz, and would be considerably improved by a more mechanically solid scheme for mounting the cavity output mirror.

Further optimization of the Q-switched Ni:MgF₂ laser⁷ produced a peak power output of 140 W in a 480-nsec output pulse at a 100-Hz repetition rate. The output energy density extraction represented by that level of power is about 1 J/cm³. The actual energy density extraction from the active medium, because of losses in the Q-switch, was closer to 4 J/cm³, about 10 percent of the energy extraction possible with all the Ni⁺² ions inverted in a 1 wt%-doped crystal. This result indicates that scaling the output of the Ni:MgF₂ laser to the 10- to 100-mJ region should be possible using excited regions 1 mm in diameter in laser crystals 2 to 5 cm long.

P. F. Moulton
A. Mooradian

C. EFFECTS OF NARROW FREE-SPECTRAL-RANGE ETALONS ON MODE-LOCKED LASERS

The effects on a homogeneously broadened forced mode-locked laser from a narrow free-spectral-range etalon inside the laser cavity have been calculated. The type of etalon under consideration has a free spectral range (FSR), F , which is narrow compared not only with the laser medium linewidth Δf , but with the mode-locked linewidth as well. Such a situation can occur, for example, in Nd:YAG (Ref. 8) or (Nd, La)P₅O₁₄ (Ref. 9) lasers having 20- and 40-GHz mode-locked bandwidths, respectively, if $F \lesssim 5$ GHz. This FSR would be obtained from an intracavity component having a 2-cm length with index of refraction 1.5. Since the etalon optical length will be much less than that of the overall optical cavity, the FSR is much greater than the cavity mode spacing. Similar regimes of operation are found in mode-locked semiconductor lasers.

The other range of etalon spacing with FSR wider than the mode-locked bandwidth has been treated by Kuizenga and Siegman⁸ using an expansion of the etalon transmission maximum near the center frequency. As expected, the additional frequency selectivity of the etalon narrows the lasing spectrum and broadens the mode-locked pulses.

The method used to evaluate the etalon modulation effects is a perturbation solution of the harmonic oscillator forced mode-locked equation derived by Haus.¹⁰ This necessarily restricts the etalon effects to be small; one of the results found below is a limit on how small the etalon modulation must be for the perturbation solution to be valid.

With zero detuning of the mode envelope from the central cavity mode, the equation for the continuum limit of the mode envelope $E(\omega)$, centered about the laser oscillation frequency, is

$$\left[2\delta_f \omega_m^2 \frac{d^2}{d\omega^2} - 4g \frac{\omega^2}{\Delta\omega^2} + \Delta g - \frac{\epsilon}{4} (1 + \cos \omega T) \right] E(\omega) = 0 \quad (\text{II-1})$$

where

δ_f = mode-locking loss modulation amplitude

ω_m = modulation (radian) frequency, $f_m = \omega_m/2\pi$

$\Delta\omega$ = laser medium (radian) linewidth, $\Delta f = \Delta\omega/2\pi$

g = saturated amplitude gain at line center

Δg = excess gain with mode-locking

T = inverse free spectral range, $1/F$

$\epsilon = 4\mathcal{R}/(1 - \mathcal{R}^2)$, where \mathcal{R} is the etalon reflectivity.

The solutions of Eq. (II-1) with $\epsilon = 0$ for the mode-locked laser are the Hermite-Gaussian "super-modes" found previously,¹¹ of which only the lowest-order Gaussian one is stable. Equation (II-1) is rewritten in normalized form

$$\frac{d^2 E}{d\omega^2} + (\lambda - \beta^2 \omega^2) E - \gamma (\cos \omega T) E = 0 \quad (\text{II-2})$$

where

$$\lambda = \frac{(\Delta g - \epsilon/4)}{(2\delta_f \omega_m^2)}$$

$$\beta^2 = \frac{2g}{(\delta_f \omega_m^2 \Delta \omega^2)}$$

$$\gamma = \frac{\epsilon}{(8\delta_f \omega_m^2)}$$

This is the harmonic-oscillator wave equation with a perturbation $-\gamma \cos \omega T$ in ω -space. Standard first-order perturbation theory can be applied directly to solve Eq. (II-2), but because of the periodic nature of the perturbation it is convenient to Fourier-transform Eq. (II-2) to the time domain

$$\frac{d^2}{dt^2} f(t) + \left(\frac{\lambda}{\beta^2} - \frac{t^2}{\beta^2} \right) f(t) - \frac{\gamma}{2\beta^2} [f(t+T) + f(t-T)] = 0 \quad (\text{II-3})$$

where $f(t)$ is the amplitude envelope of a mode-locked pulse. This is also a perturbed harmonic-oscillator wave equation, reflecting the fact that Fourier transforms of the Hermite-Gaussian solutions of Eq. (II-2) are also Hermite-Gaussian functions in the time domain. Expanding the solution of Eq. (II-3) in terms of the zero-order eigenfunctions $f_m(t)$ gives the first-order perturbation solution

$$f(t) = f_0(t) + \sum_{m=1}^{\infty} c_m f_m(t) \quad (\text{II-4})$$

with

$$c_m = -\frac{\gamma}{2(\lambda_m - \lambda_0)} \int_{-\infty}^{\infty} [f_m(t) f_0(t+T) + f_m(t) f_0(t-T)] dt \quad (\text{II-5})$$

In all the following equations, m will be even. The vanishing of odd- m terms comes from the original assumption of an even-symmetry $\cos \omega T$ perturbation.

The full-width half-maximum frequency linewidth of the unperturbed mode-locked laser intensity is

$$\Delta f_{ML} = \sqrt{2\sqrt{2} \ln 2} \left(\frac{\delta_f}{g} \right)^{1/4} \sqrt{f_m \Delta f} \quad (\text{II-6})$$

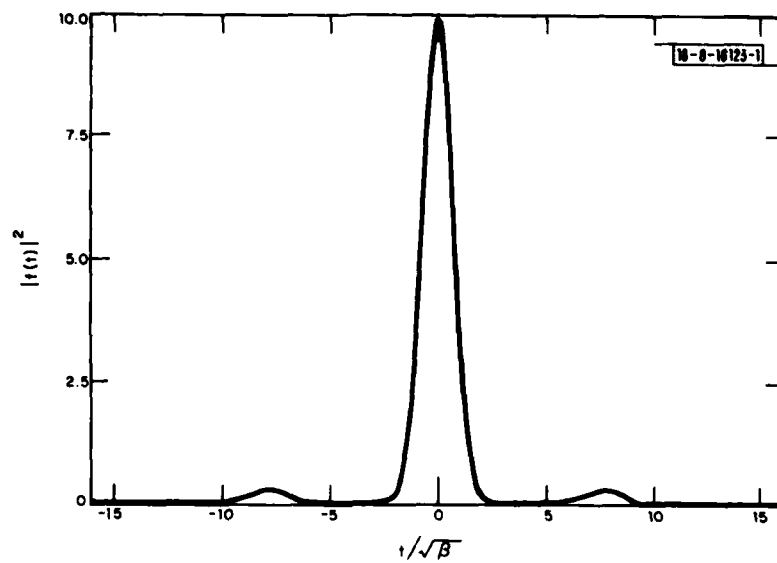


Fig. II-8. Perturbed mode-locked pulse intensity as a function of normalized time $t/\sqrt{\beta}$. Etalon FSR parameter $\rho = 8$, and etalon modulation parameter is $(\epsilon/16\sqrt{2g\delta\theta}) (\Delta\omega/\omega_m) = 10$. Unperturbed pulse coincides with central peak.

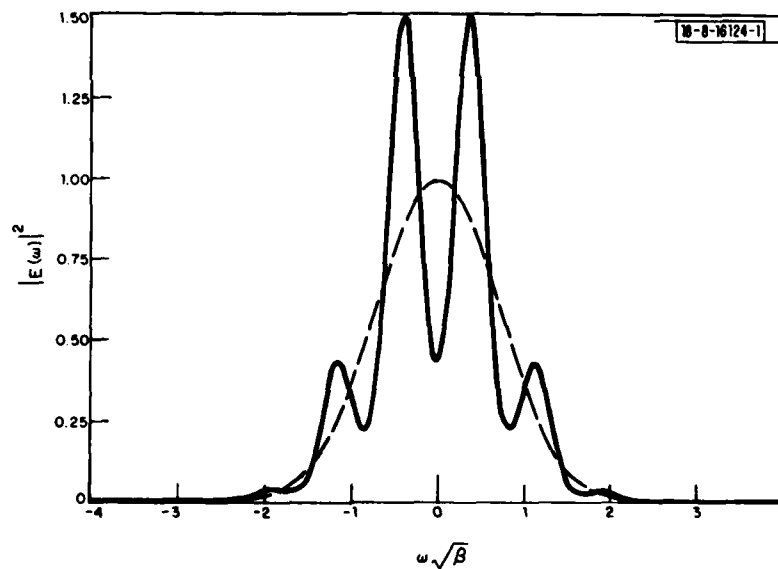


Fig. II-9. Perturbed mode-locked frequency spectrum as a function of normalized frequency $\omega\sqrt{\beta}$, with same etalon parameters as in Fig. II-8. Dashed curve is unperturbed spectrum.

and Eq. (II-5) can be expressed as

$$c_m = -\frac{\epsilon}{16\sqrt{2g\delta_f}} \left(\frac{\Delta\omega}{\omega_m}\right) \frac{1}{m\sqrt{2^m m!}} \rho^m e^{-\rho^2/4} \quad (\text{II-7})$$

where

$$\rho = \frac{T}{\sqrt{\beta}} = \frac{\pi}{\sqrt{L\lambda}} \left(\frac{\Delta f_{ML}}{F}\right)$$

In frequency space, the same form of expansion as Eq. (II-4) is found from Fourier transformation. The coefficients c_m are the same, except for an additional multiplicative factor of $(-1)^{m/2}$.

Some typical results of these calculations are shown in Figs. II-8 and II-9 for $\rho = 8$, or $\Delta f_{ML} = 2.12 F$, and $(\epsilon/16\sqrt{2g\delta_f})(\Delta\omega/\omega_m) = 10$. Figure II-8 is a plot of the time-dependent intensity of the mode-locked pulse vs normalized time $t/\sqrt{\beta}$. The frequency-dependent power spectrum is shown in Fig. II-9 as a function of normalized frequency $\omega\sqrt{\beta}$, along with the unperturbed spectrum. In both figures, the unperturbed function maxima have been set equal to unity. As expected, the etalon modulates the frequency spectrum with a period equal to the free spectral range. In the time domain, this corresponds to creation of small satellite pulses separated from the main pulse by the etalon round-trip transit time. The larger effect on the frequency spectrum occurs because the frequency perturbation is strongest near the unperturbed peak, whereas the time perturbation is located away from the main pulse. Squaring the perturbed amplitude functions then increases the perturbation deviations in the frequency domain, while reducing them in the time domain. A measured spectrum for an etalon-perturbed mode-locked Nd:YAG laser is shown in Fig. 5 of Ref. 11, and is qualitatively similar to our calculated spectrum.

From Fig. II-9 and similar calculations, it is found that the perturbed amplitude frequency spectrum can be put in the approximate form

$$E(\omega) \sim e^{-\beta\omega^2/2} (1 - \eta \cos \omega T) \quad (\text{II-8})$$

To the extent that the actual perturbation function differs from $(1 - \eta \cos \omega T)$, i.e., has higher harmonic content, additional pulses will be found in the time domain separated by $1/F$. Using the above results, it can be shown that

$$\eta \approx \frac{\epsilon}{8\sqrt{2g\delta_f}} \left(\frac{\Delta\omega}{\omega_m}\right) \frac{1}{\rho^2} = \frac{\epsilon F^2}{8\delta_f \omega_m^2} \quad (\text{II-9})$$

[The parameter η calculated using Eq. (II-9) is 0.31 for the functions shown in Figs. II-8 and II-9.] From this result, which is in excellent agreement with numerical calculations, one sees that narrowing the FSR decreases the perturbation effect. In the frequency domain, this can be interpreted as an increased tendency for cavity mode coupling across narrower potential wells, and in the time domain as greater loss for secondary pulses separated farther from the time of maximum modulator transmission.

Let us examine some examples of actual mode-locked lasers to find approximate limits on ϵ . For (Nd, La)P₅O₁₄ lasers with $\Delta f \approx 750$ GHz, typical values are $2\delta_f = 0.05$, $2f_m = 500$ MHz, and $F = 5$ GHz, giving $\epsilon \lesssim 0.02$ or $\eta \lesssim 0.005$. For a mode-locked semiconductor laser¹² with $\Delta f = 6$ GHz, the laser diode itself is the etalon located inside an external cavity. The effects of gain

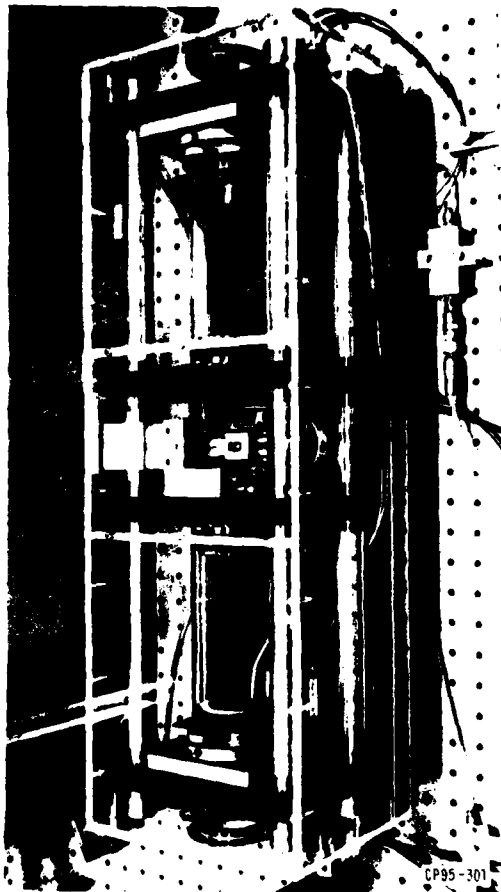
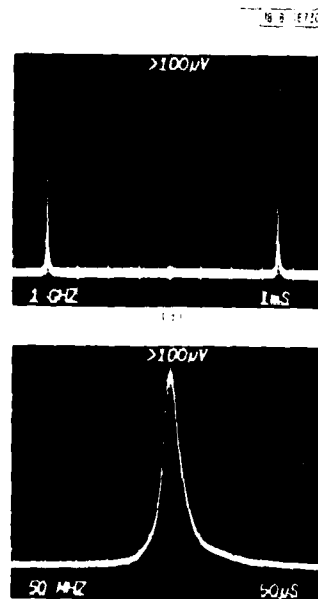


Fig. II-10. External-cavity semiconductor laser.

Fig. II-11. Fabry-Perot scanning interferometer spectrum of external-cavity laser: (a) 1 GHz/div; (b) 50 MHz/div. Asymmetry in (b) is due to detector.



modulation on the diode are assumed to be qualitatively the same as those of loss modulation. Then with $2\delta_f \approx 0.2$, $2f_m = 2$ GHz, and $F = c/2nl_{\text{diode}} = 120$ GHz, the limits on etalon modulation and reflectivity are $\epsilon \lesssim 0.002$ and $R \lesssim 5 \times 10^{-4}$. In (Nd, La)P₅O₁₄ or Nd:YAG lasers, etalon effects can be made small enough by a combination of antireflection coating and wedging intra-cavity elements, but the problem in semiconductor lasers is far more severe. Haus¹³ has examined the question of etalon effects in semiconductor lasers from the opposite viewpoint of deep etalon modulation and found qualitatively similar conclusions regarding the necessity for suppressing the etalon reflectivity. Without such suppression, in the presence of spontaneous emission noise the spectral modulation is deep enough to confine the modal phase coherence within the spectral wells, leading to uncorrelated clusters of locked modes.

S. R. Chinn

D. CHARACTERISTICS OF EXTERNAL CAVITY (Ga, Al)As DIODE LASERS

A stable, single-mode tunable external-cavity semiconductor laser has been designed and constructed. Its spectral properties have been studied in order to investigate spectral and spatial gain hole burning which are believed to contribute to the typically multimode oscillation in isolated injection lasers. In addition, the external-cavity laser has been force-mode-locked and nearly transform-limited pulse widths with grating tunability of the laser emission have been observed.

The external-cavity laser is illustrated in Fig. II-10. The particular double-heterostructure (Ga, Al)As diode used in the experiments has a p-type active layer containing approximately 8-percent Al. The diode is 200 μm long, with a 13- μm stripe defined by a selectively etched n-type GaAs current-blocking layer. The facets are antireflection coated. High stability in the diode position, which is necessary for long-term single-mode operation, is provided by a thermally compensated Invar diode translator. The diode radiation is collimated by two 50-mm $f/1.4$ antireflection-coated lenses. Tuning is accomplished with a 1200-line/mm 750-nm gold-coated grating, and the output radiation is coupled through a dielectric-coated mirror with reflectivity ranging from 10 to 40 percent. The various components are supported by four 1-in.-diam super-Invar rods, with the cavity length adjustable from 20 to 50 cm. Fine frequency tuning and mirror adjustments are accomplished by piezoelectric control. The entire laser is enclosed in a Lucite housing, which provides partial acoustic and thermal isolation and permits the laser cavity to be filled with dry nitrogen during operation.

When the emission of the external-cavity laser occurred in the fundamental transverse mode, only one axial mode was evident in scanned interferometer transmission spectra as shown in Fig. II-11(a-b), although more than ten longitudinal cavity modes could possibly oscillate within the spectral envelope of the laser grating. The mode jitter is 2 MHz and the frequency drift is 2 MHz/min. in an unstabilized cavity. The short-term (<5 min.) amplitude stability of the laser is 1 percent, and the unit operates in a single mode for up to 1 hr without mode jumps. The laser emission is tunable over a spectral range of more than 10 nm, with up to 70 percent of the original multimode stimulated power (several milliwatts) of the originally isolated diode condensed into a single mode in the external cavity, indicating the absence of spatial hole burning by longitudinal modes at power levels of a few milliwatts. Similar results were obtained for several devices.

The extent of the spectral homogeneity was investigated by directly measuring the spontaneous emission spectrum of the laser. Previous studies¹⁴⁻¹⁷ of spectral hole burning and gain saturation in semiconductor lasers were complicated by various problems inherent in experiments with isolated laser diodes, such as frequency chirping and mode competition in pulsed devices, nontunable multimode laser emission, and spectral gain shifts associated with significant variations in the injection current. The present investigation eliminated these problems by external control and stabilization of the mode characteristics of a CW laser diode.

In the experiment, the laser was tuned to a particular frequency and the spontaneous emission spectrum was recorded using a 3/4-m double monochromator and a cooled GaAs photomultiplier. A slit aperture between the laser and the spectrometer ensured that the recorded spontaneous emission originated in the fundamental lateral mode volume from which the laser power was extracted. Spectra were recorded for the diode with and without external-cavity grating feedback, and the procedure was repeated for various laser wavelengths across the gain spectrum.

The spectrometer recordings exhibited superradiant fringes due to the slight (~1 percent) reflectivity of the coated facets; however, the stimulated emission in the internal diode modes caused no significant error in the experiment, since the maximum fringe intensity was nearly three orders-of-magnitude less than the laser mode intensity. The spectra were digitized for numerical analysis, and the valleys between the fringe maxima were selected for plots of the spontaneous emission. Typical results are plotted in Fig. II-12(a). The overall amplitude reduction in the spectrum with feedback relative to that without feedback is due to the saturation of the gain at a value equal to the losses of the laser mode when the diode was allowed to oscillate in the external cavity.

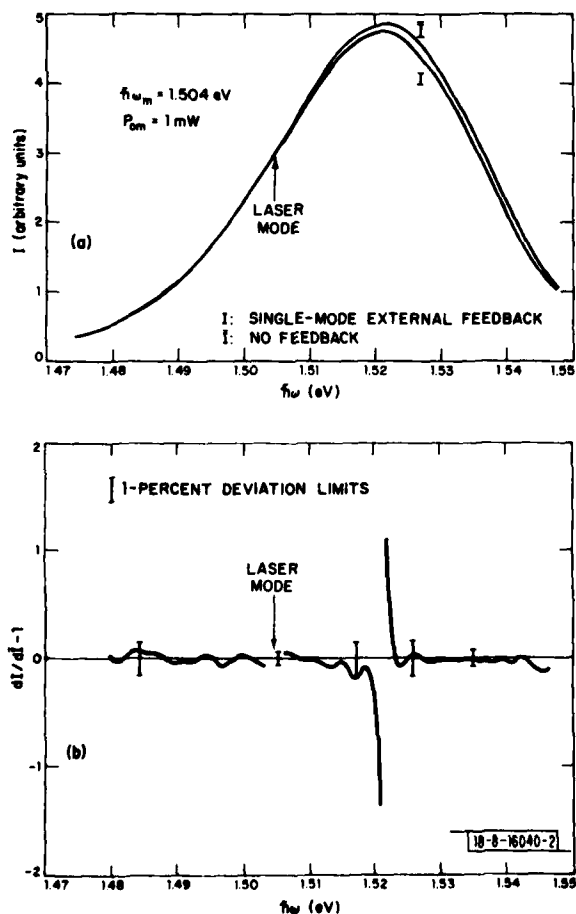


Fig. II-12. (a) Spontaneous emission spectra of external-cavity laser with and without single-mode grating feedback. (b) Ratio of derivatives of spectra in (a). Divergence at 1.522 eV coincides with emission peak, where derivatives vanish.

A sensitive indicator of deviation in the spontaneous emission spectrum with feedback relative to that without feedback is the ratio of the energy derivatives of the spectra, as plotted in Fig. II-12(b). This ratio should be close to unity unless the derivatives vanish or the spectra differ in shape over a localized range of photon energy. Within the 1-percent experimental error limits, no positive evidence of a depression in the spontaneous emission is seen in Fig. II-12(b). Considering the amplification of the spontaneous emission over the length of the diode,¹⁸ a 1-percent spontaneous-emission hole depth would correspond to a gain depression of somewhat less than 0.5 percent.

Theories^{14,19} of spectral hole characteristics generally predict an inverse proportionality of the hole width to the intraband energy relaxation time. The width ranges from ~1 nm for a relaxation time of 10^{-12} sec to ~10 nm for 10^{-13} sec. The expected depth, on the other hand, depends on the model assumed in the calculation. The hole depth has been estimated from a phenomenological calculation for a single-mode semiconductor laser with band-to-band recombination and a single energy relaxation rate for conduction-band electrons in a p-type active region. A Boltzmann equation steady-state balance of the spectral injection rate $R_{inj}(E)$, recombination rate, and intraband scattering rate τ_s yields the following expression for the occupation function of $f_c(E)$ in the conduction band:

$$f_c(E) \approx \bar{f}_c(E) \left[1 - \frac{\tau_s R_m}{\eta \rho_c(E) \bar{f}_c(E)} L(E, E_m) \right]$$

where $\bar{f}_c(E) = f_c^0(E) + \tau_s R_{inj}(E)/\rho_c(E)$, $R_m = P_m/\hbar\omega_m V$, and $L(E, E_m) = (\hbar/\pi\tau_s)/[(E - E_m)^2 + (\hbar/\tau_s)^2]$. $\bar{f}_c(E)$ is the quasithermal distribution resulting from the injection of carriers at rate $R_{inj}(E)$ into the thermal (Fermi) distribution $f_c^0(E)$. $\rho_c(E)$ is the energy density of states, R_m is the rate of stimulated emission into the laser mode, P_m is the mode power, and η is the internal radiative quantum efficiency. $L(E, E_m)$ is the lineshape function for the radiation due to a stimulated transition, originating at the energy level E_m , which is broadened to a spectral energy width $2\hbar/\tau_s$ by intraband scattering. Energies are measured from the bottom of the conduction band.

For a thermalization time of 1 psec and an emitted mode power of 2 mW, our model predicts that the gain hole depth should be ~0.1 percent. Therefore, the 0.5-percent upper limit to the gain hole depth as determined in this experiment is consistent with an estimate of $\sim 10^{-12}$ sec as the upper limit to the conduction-band thermalization time for the diode used in the investigation. The corresponding minimum spectral hole width (FWHM) is 1 nm. The tightening of experimental tolerances in future investigations is expected to result in the determination of the hole width in the range from 1 to 10 nm.

Because of the stability and tunability of the laser and the relative ease of modulating the system through microwave injection in addition to the normal DC bias current, we undertook a series of experiments to mode lock the external-cavity semiconductor laser. Previous successful efforts in mode locking of diode lasers were carried out by Ho *et al.*²⁰ in a hemispherical cavity without tunability. We achieved mode locking with a pulse width of 140 psec with a pulse repetition rate of 710 MHz at an average power output of 1 mW. The emission was tunable over a spectral range of 10 nm. The actual microwave current modulation in the diode was estimated to be 10 mA peak-to-peak; under these conditions the corresponding theoretical minimum pulse width for mode locking through a simple gain modulation of the laser is 110 psec, in reasonably good agreement with our results.

M. W. Fleming
A. Mooradian

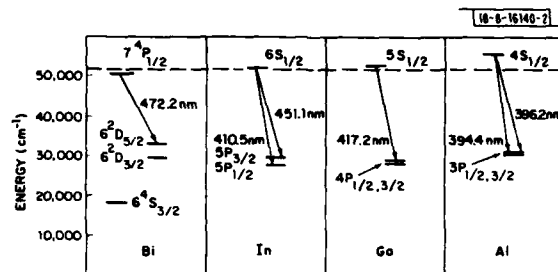


Fig. II-13. Energy-level diagram for metal-iodide-based atomic lasers. Ground-state energy of atom has been displaced upwards by dissociation energy of corresponding mono-iodide, as given in Table II-1. Dashed line at 6.4 eV corresponds to energy of ArF laser pump photon.

TABLE II-1 PROPERTIES OF METAL TRI-IODIDE-BASED LASERS				
Property	Lasing Atom			
	Bi	In	Ga	Al
Wavelength (nm) (relative intensity)	472.2	410.5 (3) 451.1 (1)	417.2	394.4 (6) 396.2 (1)
Energy Efficiency (percent)	—	1.2	2.9	0.3
Threshold Energy (J/cm ²)	0.3	0.08	0.05	0.6
Maximum Output (mJ)	0.08	0.24	0.24	0.07
Output Pulse Width (nsec)	3.2	—	4.0	4.0
Temperature (°C)	285.0	218.0	144.0	135.0

E. ATOMIC TRANSITION LASERS BASED ON TWO-PHOTON DISSOCIATION OF METAL TRI-IODIDE VAPORS

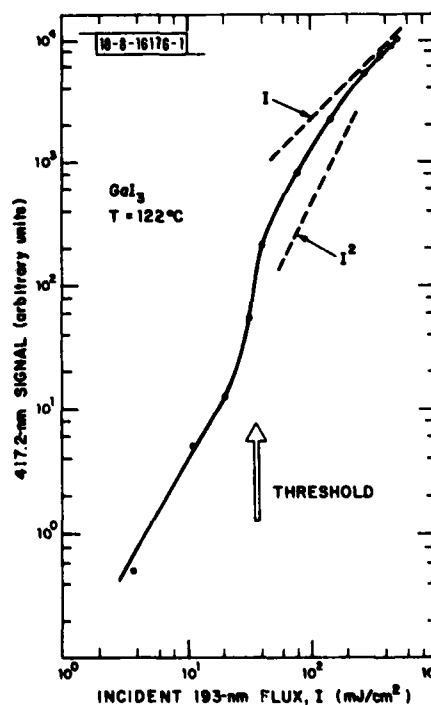
A number of metal atom lasers based on the UV laser photodissociation of vapors of the monohalide salts of In, Tl, Na (Ref. 21), K (Ref. 21), Rb (Ref. 21), and Cs (Ref. 21) have recently been reported. These atomic resonance-line lasers use a stable medium operating at moderate temperatures and have low pumping thresholds. Resonance-line lasers have the potential of being simple, inexpensive, compact high-brightness sources suitable for monitoring the presence of metal atoms. Here, we report laser action based on the photodissociation of the tri-iodide salts of Ga, In, Al, and Bi and present evidence that the excitation mechanism involves the sequential absorption of two pump photons.

The configuration for our experiments was similar to that used for studies of the TlI and alkali-halide lasers. An excimer laser provided 7-nsec-long, 193-nm ArF laser pulses with energies of up to 35 mJ. A longitudinal pumping geometry, in which the rectangular ArF laser beam was focused into a heated quartz cell containing the metal iodide, was used.

For each iodide, superfluorescent laser action was easily obtained on at least one atomic transition. The transitions involved are summarized in Fig. II-13 in which the atomic ground-state energy has been displaced upwards by the dissociation energy of the corresponding mono-iodide in order to make clear that a single 193-nm laser photon is barely energetic enough to dissociate the mono-iodide; as discussed below, another photon is needed to dissociate the tri-iodide into the mono-iodide. Table II-1 lists a number of the characteristics of these metal tri-iodide-based lasers.

Figure II-14 shows the dependence of the 417.2-nm Ga emission from the GaI_3 cell on 193-nm pump flux; the direction of observation was along the pump-beam axis. At low pump levels, the spontaneous emission is observed to have a nearly quadratic dependence on pump intensity. There is a threshold for superfluorescent emission where the emission rises more rapidly than I^2 (I is the incident flux intensity). In the lasing region, the emission returns to an I^2 dependence as the

Fig. II-14. Output emission from Ga laser ($\lambda = 417.2$ nm) vs pump intensity I above and below lasing threshold.



gain saturates. At still higher pumping intensities, the laser output varies linearly with I because of the effect of bleaching, discussed below.

On the basis of the known energetics of the tri-iodides and our experimental results, we believe that the excitation process is a sequential two-photon mechanism in which the first step is either

- (1) $MI_3 + h\nu(193 \text{ nm}) \rightarrow MI + 2I$, or
- (2) $MI_3 + h\nu(193 \text{ nm}) \rightarrow MI + I_2$, followed by
- (3) $MI + h\nu(193 \text{ nm}) \rightarrow M^* + I$.

Here, M and M* represent ground-state and electronically excited metal atoms, respectively. Table II-2 lists the energies required for some of these steps based on known thermal data. It is apparent that the energy of a single ArF photon, 6.4 eV, is insufficient to produce metal atoms in the $nS_{1/2}$ or $nP_{1/2}$ upper laser levels by dissociation of the tri-iodide. However, the energetics of Table II-2 are consistent with the two-photon sequence (1) to (3) above. Notice that

TABLE II-2 ENERGY REQUIRED FOR VARIOUS METAL-IODIDE DISSOCIATION PROCESSES				
Process	Energy (eV)			
	Bi	In	Ga	Al
$MI_3 \rightarrow MI + 2I$	3.37	3.53	3.8	4.95
$MI_3 \rightarrow MI + I_2$	1.81	1.97	2.2	3.4
$MI \rightarrow M + I$	2.25	3.43	3.4	3.77
$MI \rightarrow M^* + I$	6.29	6.45	6.47	6.91

since the dissociation step of either (1) or (2) does not require 6.4 eV, the remaining energy of the ArF photon (e.g., 2.6 eV in the case of GaI_3) can go into vibrational, electronic, and translational excitation of the photofragments. This excess energy presumably provides the additional 0.5 eV of energy required for excitation of Al via step (3) (see Fig. II-13).

The quadratic variation of the laser sidelight fluorescence with 193-nm pump light also supports two-photon excitation of the atomic laser levels. At high laser fluence, the laser output exhibits a linear variation with input. Such behavior is characteristic of a sequential process in which one absorption step becomes saturated while the other continues to follow Beer's law. One-step saturation would be expected if one portion of the process has a higher optical cross section than the other. In the case of the Group IIIa trihalides, the available data²¹ suggest that the cross section for step (3) ($\sim 10^{-17} \text{ cm}^2$) is much greater than that for (1) or (2), which is estimated to be $\sim 10^{-18} \text{ cm}^2$ from our absorption measurements. Thus, the linear region shown in Fig. II-14 is consistent with the bleaching of step (3)

Many metals form both stable mono-iodide and stable higher-iodide vapors. In the present work we find that tri-iodide lasers, although they have required two-photon excitation at our pump wavelength, can operate at an efficiency comparable to (about one-half of) that of lasers based on mono-iodide salts. For excitation at near-UV wavelengths, the higher-iodide salts will be characterized by higher thresholds because of the multiphoton pumping that is required. However, this disadvantage can be offset by a significant reduction in operating temperature which accompanies the greater volatility of the higher iodides.²² The demonstration of simply obtained and efficient laser action in the tri-iodide salts significantly increases the range of candidate materials for resonance-line lasers.

T. F. Deutsch
D. J. Ehrlich
R. M. Osgood, Jr.

F. ULTRAVIOLET LASER PHOTODEPOSITION OF METAL ATOMS

In the initial experiments of this project,²³ the feasibility of UV laser photodeposition was established. A number of parametric studies have now been performed to place the previous results on a more quantitative basis.

One of the parameters needed to analyze deposition results is the optical cross section, at the laser wavelength, of the parent molecule used in photodissociation. This was obtained by measuring the optical transmission in the UV as a function of gas pressure. Figure II-15 shows typical transmission curves for DMCD [dimethyl cadmium, $(\text{CH}_3)_2\text{Cd}$] and TMAI [trimethyl aluminum, $(\text{CH}_3)_3\text{Al}$]. Plots of the natural log of the transmission vs laser power were linear for DMCD and DMZn; for TMAI, however, straight-line plots were not obtained despite numerous measurements and the use of two different bottles of TMAI. The 257-nm absorption coefficient of TMAI is estimated from the absorption at 10 Torr, which is only ~1 percent (Fig. II-15). Table II-3 summarizes these results.

Parametric studies of the CW deposition process for Cd and Al were performed using the experimental setup shown in Fig. II-16 and described in detail in Ref. 23. Measurements of deposition rate were obtained from the time dependence of the transmitted signal, as described previously.

The dependence of the deposition rate on pressure was examined at a flux of 0.1 W/cm^2 at 257 nm and found to be linear over the range 0.5 to 3.0 Torr for DMCD and 1 to 8 Torr for TMAI. Figure II-17 shows the data for DMCD.

Figure II-18 shows the results of measurements of deposition rates vs intensity at 257 nm for He-buffered DMCD and TMAI. In each case, the rates are linear in flux over the range covered, up to 2 W/cm^2 for Cd and 500 W/cm^2 for Al. Deviations from linearity are observed at high flux levels and will be discussed below. The slopes of these curves give the deposition rate per Torr of metal alkyl, and per unit intensity for Cd and Al. The rate for Cd is ~3000 times greater than that for Al; this difference is primarily due to the fact that the cross section for DMCD is at least 500 larger than that for Al (Table II-3).

Since, at high incident power, molecules are removed from the focal region by photodissociation at a rate greater than that at which they are replenished by diffusion, bleaching will occur, and a linear dependence of dissociation rate on flux would no longer be expected. The onset of bleaching should depend on the incident flux, the number of molecules in the focal region (determined by reagent pressure), the diffusion length (determined by buffer gas pressure), and

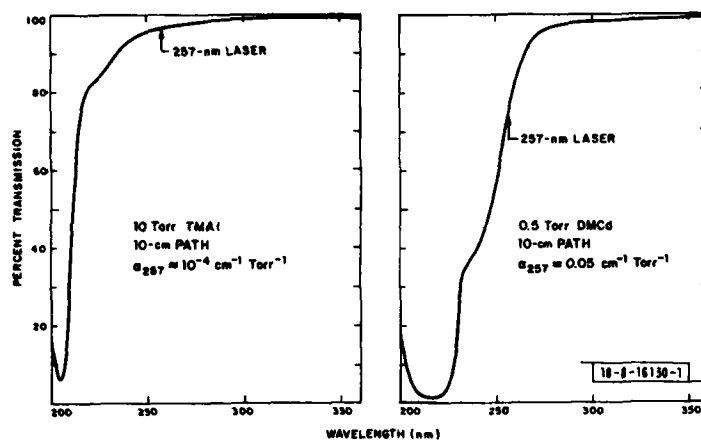


Fig. II-15. Optical transmission of TMAI and DMCD.

TABLE II-3 OPTICAL ABSORPTION COEFFICIENTS, OPTICAL CROSS SECTIONS, AND DEPOSITION RATES AT 257 nm FOR THREE METAL ALKYLs			
	DMCd	DMZn	TMAI
$\alpha_{257} \text{ (cm}^{-1} \text{ Torr}^{-1}\text{)}$	0.05	0.5×10^{-3}	10^{-4}
$\sigma_{257} \text{ (cm}^2\text{)}$	1.4×10^{-18}	1.4×10^{-20}	3×10^{-21}
Deposition Rate at 257 nm ($\text{\AA-cm}^2/\text{sec-W-Torr}$)	1.7	Not measured	5.6×10^{-4}

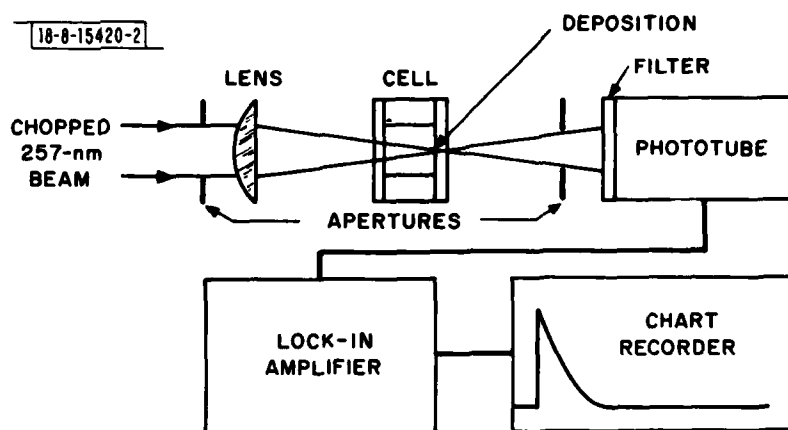


Fig. II-16. Schematic diagram of experimental system.

Fig. II-17. Cadmium deposition rate vs DMCD pressure.

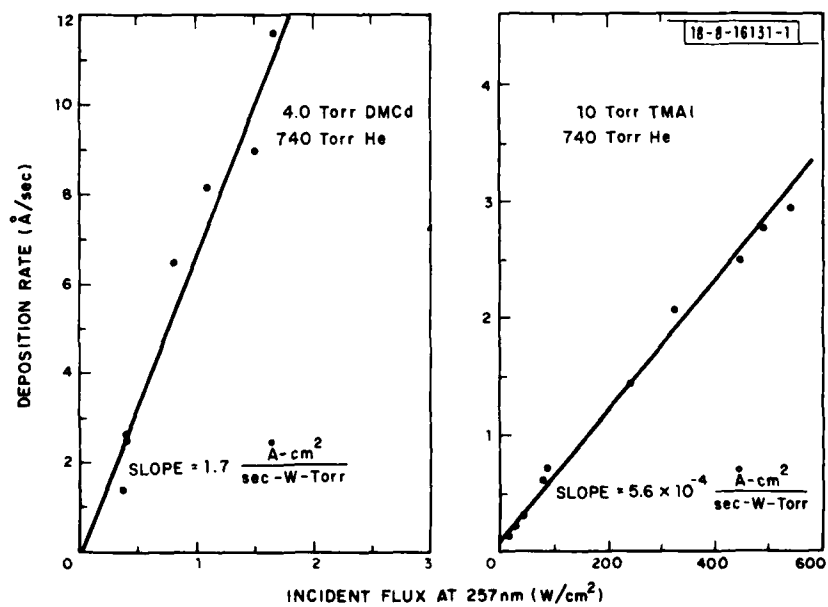
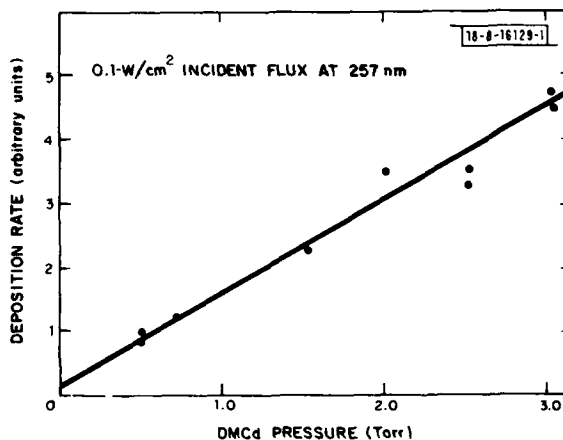


Fig. II-18. Deposition rate vs incident flux for Cd and Al using gas samples of DMCD and TMAI with He buffer gas.

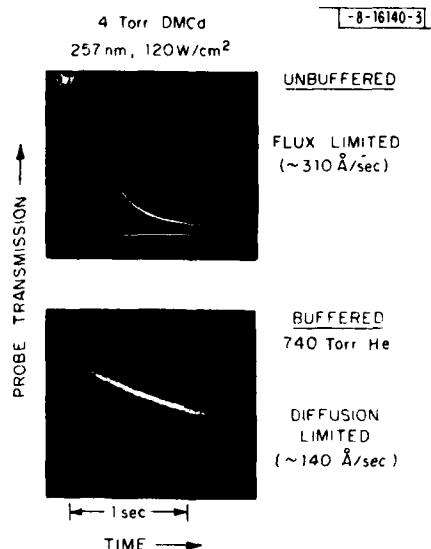


Fig. II-19. Effect of helium buffering on cadmium deposition rate.

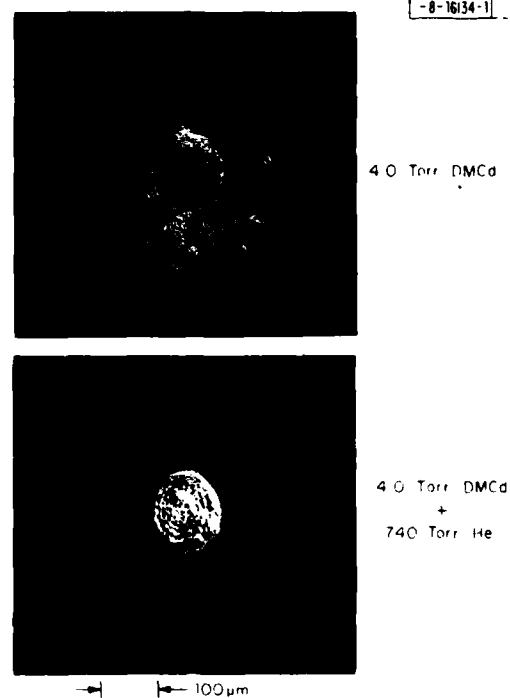


Fig. II-20. Effect of helium buffering on deposition profile. Flux is 0.3 W/cm^2 .

the size of the focal region that must be replenished by diffusion. Such effects have been observed in mixes of 4 Torr DMCd and 740 Torr He buffer gas using focal-spot sizes of $100 \mu\text{m}$. Some indications of a deviation from a linear dependence of deposition rate on flux are observed at powers of $\sim 10 \text{ W/cm}^2$. The effect of bleaching is clearer at higher fluxes; Fig. II-19 shows the time dependence of the transmission of the 257-nm beam, which monitors the deposition, for 4 Torr DMCd with and without the buffer gas, at a flux of 120 W/cm^2 . Without the buffer gas the deposition rate is $\sim 310 \text{ Å/sec}$, about a factor of 2.5 lower than the value that would be obtained using extrapolation from the low fluence value in Table II-3. When 740 Torr of He buffer is added, the reduced diffusion length leads to a diffusion-limited rate of 140 Å/sec . These experiments clearly show that at sufficiently high dissociation rates bleaching can be a significant rate-limiting step. However, this problem can be eliminated readily by using a flowing-gas system that relies on convection to transport gas into the focal region.

A helium buffer was first introduced in order to sharpen the deposition profile by reducing the diffusion of metal atoms outside the focal region. Figure II-20 shows that the addition of a helium buffer eliminates the "halo" effect found with the unbuffered cell.

D. J. Ehrlich
T. F. Deutsch
R. M. Osgood, Jr.

G. TUNABLE SUBMILLIMETER SOURCES APPLIED TO KINETICS AND RELAXATION PROCESSES IN THE FIRST EXCITED ν_3 STATE OF CH_3F

The application of a tunable submillimeter sideband spectrometer to an infrared-submillimeter double-resonance investigation of the rotational levels of CH_3F was described in a previous report.²⁴ The tunable submillimeter radiation was generated as a laser sideband and coherently

detected using Schottky-diode mixers. The very high IF frequencies of these diode mixers have now been used to investigate kinetics and relaxation processes in the excited ν_3 vibrational state of CH_3F . Three types of mechanisms were observed: stimulated emission, collisional energy transfer, and superfluorescence.

A TEA CO_2 laser was used to populate $J = 12$ rotational levels of the ν_3 vibrational state of CH_3F by optical pumping. The pulsed laser provided 200-nsec wide, 300-kW peak-power pulses on the 9.6- μm P(20) CO_2 -laser line, which was grating-tuned to maximum absorption by the CH_3F sample. The time dependence of the transmission through the sample cell of both the submillimeter laser beam and the tunable sideband beam was coherently detected, and the IF signal was sampled by a transient digital recorder.

Stimulated emission was seen when the $(\nu_3, J, K) = (1, 12, 2) \rightarrow (1, 11, 2)$ transition was directly driven by the 496- μm CH_3F laser line. In this case, sidebands of the 496- μm laser line were used as the local oscillator to demodulate the transmission of the laser beam. A large stimulated-emission pulse coincident with the pump pulse from the TEA laser was observed. A graph of the stimulated-emission pulse followed by the exponential decay of the absorption of the submillimeter laser beam at a CH_3F pressure of 25 mTorr is shown in Fig. II-21(a). Optical nutation²⁵ driven by the pump pulse was not seen since the Rabi flopping frequency was much higher than the 30-MHz bandwidth of the IF filters.

The exponential decay of the absorption of sideband beams was also observed. Figure II-21(b) shows the decay of the absorption of a sideband tuned to the $(J, K) = (7, 2) \rightarrow (8, 2)$ transition at a pressure of 1.19 Torr. Decay rates of 30 to 52 msec^{-1} were observed for this transition over the pressure range of 0.1 to 1.2 Torr. The largest contribution to the measured decay rates came from collisional redistribution of energy among internal degrees of freedom of the CH_3F . The contribution to the decay rates from both the known coupling of internal and translational degrees of freedom and diffusion of excited-state molecules out of the probe beam was small.²⁶ The decay rates did not have a simple dependence on pressure, and their interpretation was complicated by the fact that the TEA laser could pump several K levels of the $\nu_3, J = 12$ rotational state. It is clear, however, that the use of low-power, Q-switched pulsed lasers, which can populate a single K level, and Schottky-diode reradiation techniques will permit the detailed analysis of the rotational kinetics of optically pumped molecules.

Superfluorescence directly from the $J = 12$ level was also observed. The intensity of the superfluorescence depended upon the CH_3F pressure and upon tuning the TEA laser to pump efficiently the CH_3F , and did not depend upon the frequency of the probe beam. In this case, the signal at the superfluorescence frequency modulated the mixing of ν_{laser} and $\nu_{\text{laser}} \pm \nu_{\text{IF}}$ to generate the IF. As a result, the detected superfluorescence pulse had the same sign as an absorption signal. Figure II-21(c) shows the effect of a superfluorescence pulse followed by decay of the absorption of the sideband beam tuned to the $(J, K) = (7, 2) \rightarrow (8, 2)$ transition. The onset of the pulse was coincident with the pump pulse, and the width of the superfluorescence pulse was about 400 nsec over the pressure range 0.1 to 0.6 Torr.

W. A. M. Blumberg D. D. Peck
H. R. Fetterman P. F. Goldsmith[†]

[†] University of Massachusetts, Amherst.

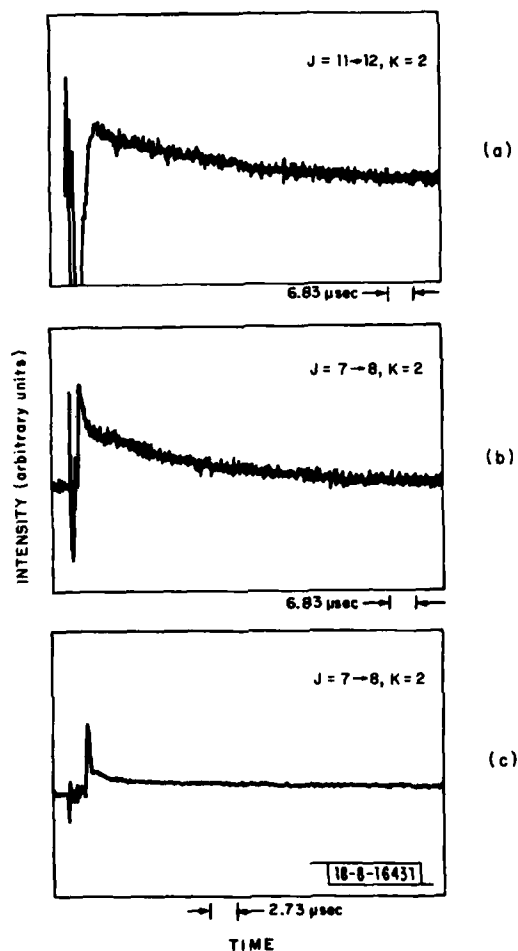


Fig. II-21. (a) Stimulated-emission pulse followed by absorption of CH_3F submillimeter laser beam at pressure of 25 mTorr. (b) Absorption of sideband beam tuned to $(\nu_3, J, K) = (1, 7, 2) \rightarrow (1, 8, 2)$ transition at pressure of 1.19 Torr. (c) Superfluorescence pulse followed by absorption of sideband beam tuned to $(\nu_3, J, K) = (1, 7, 2) \rightarrow (1, 8, 2)$ transition at pressure of 1.19 Torr.

REFERENCES

1. Solid State Research Report, Lincoln Laboratory, M.I.T. (1978:3), p. 7, DDC AD-A065116/6.
2. L. F. Johnson, R. E. Dietz, and H. J. Guggenheim, Appl. Phys. Lett. 5, 21 (1964).
3. Solid State Research Report, Lincoln Laboratory, M.I.T. (1978:1), p. 20, DDC AD-A056715/6.
4. P. F. Moulton, "Design Considerations for a Single Frequency YAG Laser," MS Thesis, Department of Electrical Engineering and Computer Science, Massachusetts Institute of Technology (14 May 1971).
5. H. G. Danielmeyer, in Lasers, edited by A. K. Levine and A. J. DeMaria (Dekker, New York, 1976), Vol. 4, Chap. 1, p. 58.
6. H. W. Schroder, H. Dux, and H. Welling, Appl. Phys. 7, 21 (1975).
7. Solid State Research Report, Lincoln Laboratory, M.I.T. (1978:4), p. 18, DDC AD-A068563.
8. D. J. Kuizenga and A. E. Siegman, IEEE J. Quantum Electron. QE-6, 694 (1970).
9. S. R. Chinn and W. K. Zwicker, Appl. Phys. Lett. 34, 847 (1979).
10. H. A. Haus, IEEE J. Quantum Electron. QE-11, 323 (1975).
11. A. E. Siegman and D. J. Kuizenga, Opto-Electron. 6, 43 (1974).
12. P. T. Ho, L. A. Glasser, E. P. Ippen, and H. A. Haus, Appl. Phys. Lett. 33, 241 (1978).
13. H. A. Haus, private communication.
14. Y. Nishimura, K. Kobayashi, T. Ikegami, and Y. Suematsu, Rep. IECE of Japan Tech. Group on Quantum Electronics, QE71-22 (1971).
15. P. Brosnon, J. E. Ripper, and N. B. Patel, IEEE J. Quantum Electron. QE-9, 273 (1973).
16. M. Nakamura, K. Aiki, and J. Umeda, Appl. Phys. Lett. 32, 322 (1978).
17. N. B. Patel, P. Brosnon, and J. E. Ripper, Appl. Phys. Lett. 34, 330 (1979).
18. E. I. Gordon, Bell Syst. Tech. J. 43, 507 (1964).
19. B. Zee, IEEE J. Quantum Electron. QE-14, 727 (1978).
20. P.-T. Ho, L. A. Glasser, E. P. Ippen, and H. A. Haus, Appl. Phys. Lett. 33, 241 (1978).
21. D. J. Ehrlich and R. M. Osgood, Jr., Appl. Phys. Lett. 34, 655 (1979).
22. R. F. Rolsten, Iodide Metals and Metal Iodides (Wiley, New York, 1961).
23. T. F. Deutsch, D. J. Ehrlich, and R. M. Osgood, Jr., Appl. Phys. Lett. 35, 175 (1979).
24. Solid State Research Report, Lincoln Laboratory, M.I.T. (1979:1), p. 30, DDC AD-A073152.
25. R. L. Shoemaker, Laser and Coherence Spectroscopy, edited by J. I. Steinfeld (Plenum Press, New York, 1978).
26. J. Preses and G. W. Flynn, J. Chem. Phys. 66, 3112 (1977).

III. MATERIALS RESEARCH

A. GROWTH OF GaAs EPILAYERS ON LARGE-GRAINED GaAs SUBSTRATES

Having achieved conversion efficiencies exceeding 20 percent at AM1 for GaAs solar cells with a shallow-homojunction $n^+/p/p^+$ structure prepared by chemical vapor deposition (CVD) on single-crystal substrates,^{1,2} we are now developing the technology for producing efficient cells of this type on low-cost substrates. Layers of GaAs deposited on the low-cost substrates investigated so far (e.g., metals, graphite, glass) are very fine-grained. Because the CVD growth process is dependent on crystallographic orientation,³⁻⁵ these layers exhibit variations in surface topography and impurity doping that may contribute to poor solar cell performance, either by degrading the GaAs material properties or by interfering with cell fabrication. To address these problems we have examined the effect of orientation on growth rate, surface morphology, and impurity segregation of CVD-grown layers. Our approach has been to utilize GaAs substrates with sufficiently large grains to permit the orientation, thickness, and doping of the different grains in the grown layers to be found by standard techniques, which are not applicable to very small grains. The experiments have shown that the variations in surface topography resulting from differences in orientation can be minimized by adjusting the growth parameters, and also that variations in impurity doping from grain-to-grain are small enough to be compatible with the techniques that we have developed for fabricating shallow-homojunction GaAs cells on single-crystal substrates.

Epitaxial layers of GaAs were deposited at 730°C on p^+ -substrates in an $AsCl_3$ -Ga- H_2 vertical CVD system similar to one described previously.² The $AsCl_3$ was maintained at 15°C, and the Ga source at 830°C. Growth rates from 1.2 to 31 $\mu\text{m/hr}$ were obtained by decreasing the H_2 flow through the $AsCl_3$ evaporator from 600 to 100 cm^3/min . In most runs, a p-layer about 5 μm thick (doped with Zn between 5×10^{16} and $4 \times 10^{17} \text{ cm}^{-3}$) and an n^+ -layer about 0.1 μm thick (doped with S between 2 and $5 \times 10^{18} \text{ cm}^{-3}$) were grown in succession, as in the preparation of $n^+/p/p^+$ solar cells, but in several cases a p-layer was deposited without an n^+ -layer to facilitate measurement of the p-doping. The sources of Zn and S were dimethylzinc and H_2S , respectively. Large-grained substrates were sliced from a boat-grown ingot of Zn-doped GaAs, then lapped, polished, and etched before use to reduce surface variations to less than 0.1 μm . Included in each growth run with the polycrystalline substrate was a single-crystal wafer oriented 2° off (100) toward (110). The epilayer formed on this wafer was used as a standard for comparisons of growth rates and doping levels.

The grains studied ranged in area from 1 mm^2 to over 1 cm^2 . Their orientations were determined from Laue x-ray diffraction patterns. The orientations found are indicated schematically in Fig. III-1 by means of points plotted on a triangular section of a (100) stereographic projection. The three major planes in the cubic system are at the corners of this section, whose sides are major zone axes. The symmetry of the various orientations can be readily identified: the highest symmetry planes lie on the major zone axes, while the lowest symmetry planes lie in the central region away from the axes. The points plotted in Fig. III-1 show that most of the grains encountered had low-symmetry orientations, which have not previously been the subject of studies on CVD growth reported in the literature.

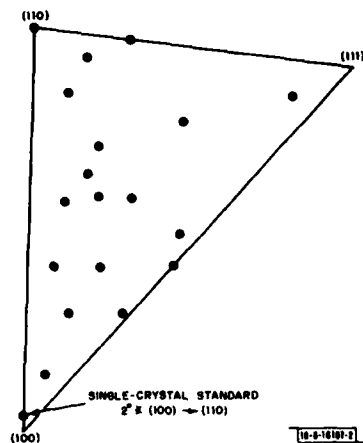


Fig. III-1. Stereographic projection showing orientations of GaAs grains studied in CVD growth experiments.

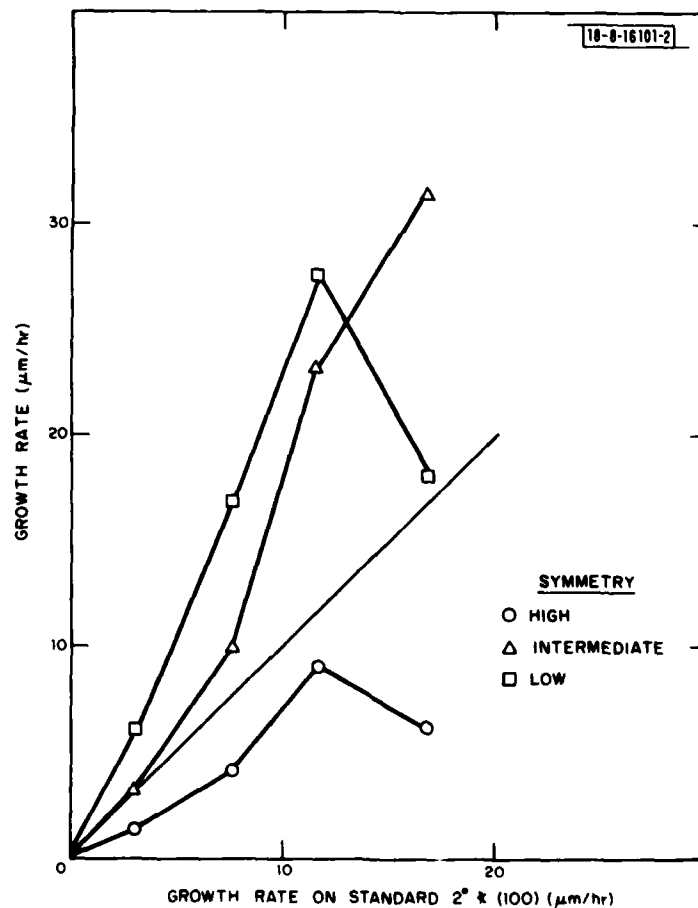


Fig. III-2. Growth rates of GaAs grains with three different orientations as a function of growth rate on standard single-crystal wafer.

In the growth-rate experiments it was found that in a single run the layer thickness was constant within each grain, but the growth rate varied markedly with orientation. When the growth rate on the standard GaAs single crystal did not exceed $8 \mu\text{m/hr}$, grains exhibiting relatively high growth rates were found to have orientations far from the major zone axes, while grains with relatively low growth rates had orientations very close to certain high-symmetry, low-index planes on the zone axes. For the remaining grains, which had intermediate growth rates, the orientations fell close to the major zone axes. Growth rates of grains in the low-symmetry group varied from $1\frac{1}{2}$ to $2\frac{1}{2}$ times the rate on the standard crystal, while the high-symmetry grains had growth rates between $\frac{1}{3}$ and $\frac{3}{4}$ of the standard rate.

For growth rates on the standard crystal greater than $8 \mu\text{m/hr}$, the above correlation between growth rate and orientation breaks down. This effect is illustrated in Fig. III-2, where the growth rates of three grains, one belonging to each of the three symmetry groups, are plotted as a function of the standard rate. At low growth rates, the correlation is shown by the constant slopes of the three plots relative to the straight line at 45° , representing the standard rate. At higher standard rates, both the high- and low-symmetry grains decreased in growth rate, while the rate of the grain with intermediate orientation [4° off (210)] increased faster than the standard rate. Growth rates for grains of other orientations were within the limits shown in Fig. III-2. The observed deviation from linear dependence on the standard rate is advantageous because it provides an opportunity for minimizing growth-rate variations from grain-to-grain by adjustment of the growth parameters. This is illustrated by Fig. III-3, where the growth

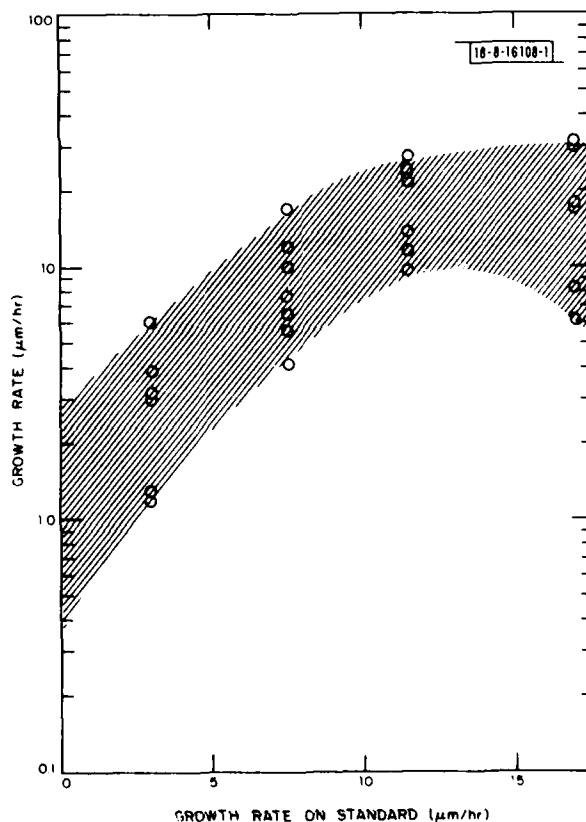


Fig. III-3. Growth rates of GaAs grains with various orientations as a function of growth rate on standard wafer.

rates for a single set of grain orientations, measured in a series of runs on adjacent substrates from the same large-grained ingot, are plotted on a logarithmic scale as a function of the standard rate. The width of the shaded region at any standard growth rate thus represents the ratio of maximum-to-minimum growth rates for all the grains. This ratio is 6 at low growth rates, decreasing to a minimum of 3 and then increasing to 6 as the standard rate increases.

In the course of the growth-rate experiments, we observed that the surface morphology of the CVD layers was also dependent on orientation. Grains with high or intermediate symmetry had rather smooth surfaces, while pits or hillocks were present on low-symmetry grains. These surface defects generally increased in density with increasing growth rate, but their morphology did not change appreciably.

The carrier concentrations in p-layers grown on the large-grained substrates, as determined by C-V measurements on grains of various orientations and normalized to the doping measured for layers grown on the standard wafers, are plotted in Fig. III-4 against the standard growth rate. For a given standard rate, the variation in p-doping from grain-to-grain was less than ± 20 percent. However, the average doping was only from $\frac{1}{4}$ to $\frac{1}{2}$ that for the layer on the standard wafer; this difference appears to be due to anomalous segregation of Zn in CVD growth on surfaces near the (100) orientation. The variation in p-doping is well within the tolerance permitted by our present solar-cell-fabrication techniques.

A detailed investigation of n^+ -doping was not made because the concentration of 4 to $5 \times 10^{18} \text{ cm}^{-3}$ used in solar cells yields ohmic contacts instead of the Schottky barriers needed for C-V measurements. For one run at a standard growth rate of about $5 \mu\text{m/hr}$, the n^+ -doping was lowered sufficiently to permit C-V measurements. As shown in Fig. III-4, the concentrations

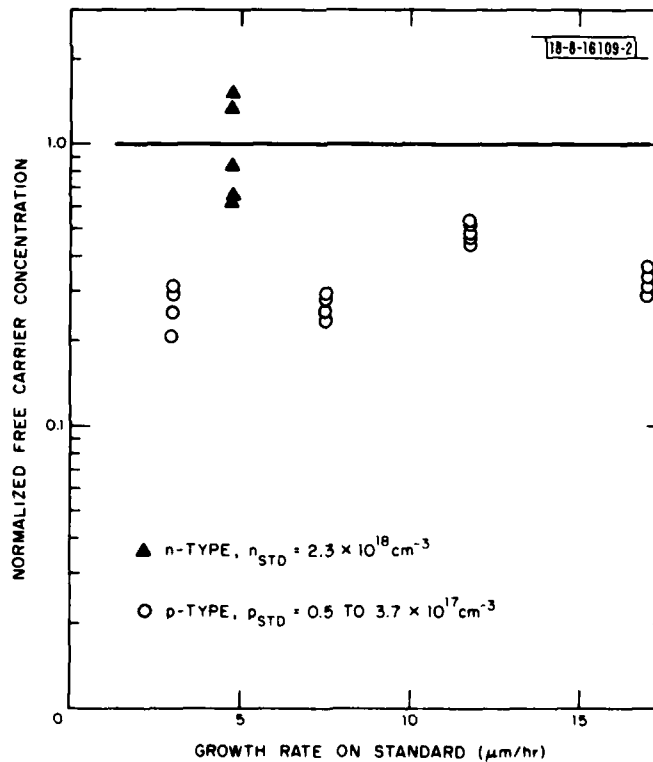


Fig. III-4. Carrier concentrations in GaAs grains with various orientations, normalized to concentrations in layers grown on standard wafers, as a function of growth rate on standard wafer.

in different grains varied by ± 50 percent from the level in the layer grown on the standard substrate, but at the higher concentrations used in practice, such a variation would not interfere with the formation of ohmic contact to the metal collection fingers.

R. P. Gale J. C. C. Fan
F. M. Davis C. O. Bozler

B. GaAs SOLAR CELLS WITH HIGH RESISTANCE TO 1-MeV ELECTRON RADIATION

Although Si solar cells have been extensively used in space, GaAs cells are now emerging as promising candidates for space applications, with a number of potential advantages over Si cells. Since the absorption length for sunlight in GaAs is only about $2\text{ }\mu\text{m}$ (see Ref. 6), two orders-of-magnitude less than in Si, GaAs cells should exhibit less radiation damage in space, because damage generated more than a few absorption lengths beneath the surface should have little effect on photocurrent collection. In addition, the theoretical conversion efficiency is higher for GaAs than for Si (see Ref. 7), and GaAs cells operate better than Si cells at elevated temperatures⁷ and high solar concentrations.⁸ Furthermore, the stronger absorption of sunlight in GaAs should allow a significant reduction in cell thickness, and therefore weight. We report here the results of initial experiments on the resistance of shallow-homojunction GaAs cells to 1-MeV electron radiation. These results are highly encouraging, suggesting that such cells would be very resistant to radiation of the space environment.

The GaAs solar cells that have been under development for space applications are mainly GaAlAs/GaAs heteroface cells,⁹⁻¹¹ which incorporate a Zn-doped¹⁰ or Be-doped¹¹ p-GaAlAs window layer grown by liquid-phase epitaxy on an n-GaAs wafer. During growth of the window layer, the p-dopant diffuses into the n-substrate producing a p-n homojunction generally more than $0.5\text{ }\mu\text{m}$ deep. The layer of GaAlAs greatly reduces the recombination velocity at the GaAs surface while transmitting almost all the solar spectrum. Single-crystal heteroface cells have been fabricated with conversion efficiencies as high as 21 to 22 percent at AM1.¹² However, irradiation with high-energy electrons, the most important source of radiation damage to solar cells in the space environment, causes a strong decrease in the photocurrent, partly because the diffusion lengths of minority carriers in the p- and n-layers are decreased and partly because the surface recombination velocity at the GaAlAs/GaAs interface is increased.¹⁰ These detrimental effects can be greatly reduced by fabricating GaAs solar cells that utilize a shallow-homojunction $n^+/p/p^+$ structure without a GaAlAs layer.

We have recently developed such shallow-homojunction solar cells, with conversion efficiencies exceeding 20 percent at AM1, that incorporate GaAs layers grown by chemical vapor deposition on either GaAs (Ref. 1) or Ge (Ref. 2) single-crystal substrates. In these devices, surface recombination losses are reduced because the n^+ -layer - doped with S - is so thin ($<1000\text{ }\text{\AA}$) that most of the photogenerated carriers are created in the p-layer - doped with Zn - below the junction. Because the n^+ -layer is so thin, almost all the electron damage effects will occur in the p-layer, where the minority carrier diffusion length is much longer ($\sim 20\text{ }\mu\text{m}$) than the solar absorption length ($\sim 2\text{ }\mu\text{m}$). Thus, the n^+/p configuration should be considerably more radiation resistant than the p^+/n configuration because the diffusion length in GaAs is much longer for electrons than for holes. We have confirmed this superior radiation resistance in a series of experiments using 1-MeV electrons at total fluences up to $1 \times 10^{16}\text{ e/cm}^2$, which should be equivalent in damage to exposure for many years in space.

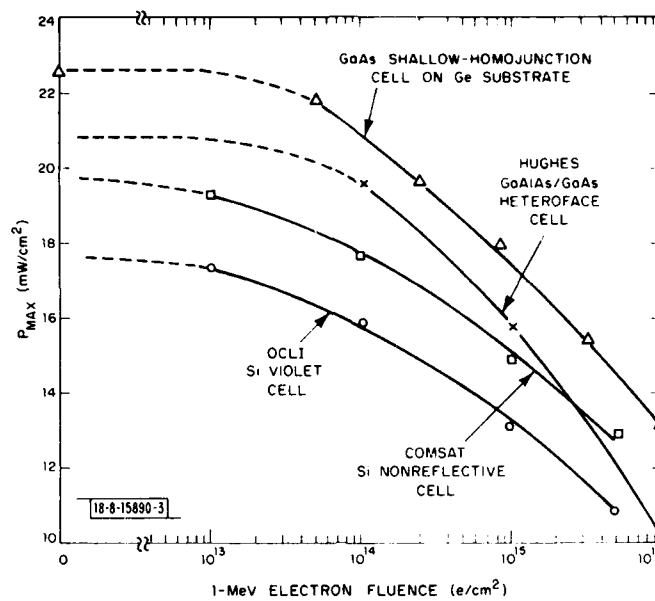


Fig. III-5. Maximum output power density at AM0, P_{max} , for Cell 1 as a function of cumulative electron fluence. Results for three other types of cells are included for comparison.

TABLE III-I
DEVICE CHARACTERISTICS OF FOUR SHALLOW-HOMOJUNCTION GaAs SOLAR CELLS
BEFORE AND AFTER 10^{16} e/cm^2 1-MeV ELECTRON IRRADIATION

Cell No.	Initial Values				Final Values (after 10^{16} e/cm^2)			
	J_{sc} (mA/cm ²)	V_{oc} (V)	ff	η (percent)	J_{sc} (mA/cm ²)	V_{oc} (V)	ff	η (percent)
1	27.5	1.00	0.82	16.7	21.0	0.82	0.77	9.8
2	19.2	0.95	0.81	10.9	18.0	0.72	0.69	6.6
3	22.0	0.99	0.80	12.9	17.2	0.82	0.76	7.9
4	25.6	0.98	0.83	15.4	17.9	0.81	0.78	8.4

Legend:

- J_{sc} = short-circuit current density
- V_{oc} = open-circuit voltage
- ff = fill factor
- η = conversion efficiency

Four $n^+/p/p^+$ GaAs cells, each about 0.5 cm^2 in area, were tested. Electron irradiation at normal incidence was provided by a Dynamitron electron accelerator. Samples were irradiated individually by mounting them next to the aperture of a Faraday cup so that all fluences were measured directly. The cells were open-circuited and at room temperature during irradiation. The electron flux density was kept at about $10^{12} \text{ e/cm}^2 \text{ sec}$, low enough to avoid significant cell heating. Cell conversion efficiencies before and after irradiation were measured at about 25°C with a solar simulator consisting of a filtered xenon source. Quantum efficiency measurements were made in a spectrometer at wavelengths from 0.40 to $0.90 \mu\text{m}$. No thermal annealing was employed between successive electron irradiations, and no self-annealing effects were observed during the time intervals between irradiations.

Figure III-5 shows the maximum output power density at AM0, P_{max} , for Cell 1 (grown on a Ge substrate) as a function of cumulative electron fluence. The value of P_{max} was initially over 22 mW/cm^2 (cell conversion efficiency η at AM0 was 16.7) and slowly decreased to about 15 mW/cm^2 at a fluence of 10^{16} e/cm^2 . Both initial and final P_{max} values are higher than those reported^{13,14} for three other types of space cells, as plotted in Fig. III-5. The results for the other three types, a GaAs heteroface cell and two Si cells, were obtained under similar experimental conditions, except that their areas were 4 cm^2 and the Si cells were thermally annealed at 50°C for over 24 hr between successive electron irradiations.¹³

Table III-1 lists device characteristics of Cell 1 before electron irradiation and after 10^{16} e/cm^2 irradiation. Although the cell exhibits excellent radiation resistance compared with other types of cells, the values of short-circuit current density J_{sc} and open-circuit voltage V_{oc} both decreased about 20 percent after the high electron fluence. The decrease in V_{oc} corresponds to an increase in leakage current, as indicated by an increase in saturation current density J_0 for the injected current component from 6×10^{-18} to $1 \times 10^{-14} \text{ A/cm}^2$ after 10^{16} e/cm^2 irradiation. The decrease in J_{sc} may be attributed partly to degradation of the electron diffusion length in the p-layer of the cell and partly to a visible change in the anodic antireflection (AR) coating. We therefore expected the J_{sc} decrease to be reduced by lowering the doping level in the p-layer below the value of $1 \times 10^{17} \text{ cm}^{-3}$ used in Cell 1, in order to increase the initial electron diffusion length, and by omitting the anodic AR coating.

Our expectation was confirmed by the results for Cell 2 (grown on a GaAs substrate) which has a p-doping level of 10^{15} to 10^{16} cm^{-3} and no anodic AR coating. Figure III-6(a) shows the device characteristics of this cell after successive electron irradiations, while the initial and final values are listed in Table III-1. For a fluence of 10^{16} e/cm^2 , J_{sc} decreased by only about 6 percent of its original value. This small decrease is confirmed by the quantum-efficiency measurements on the cell at various electron fluences, as plotted in Fig. III-6(b). The cell, however, still exhibits a significant decrease in V_{oc} . In this case, J_0 increased greatly from 2×10^{-18} to $1 \times 10^{-11} \text{ A/cm}^2$.

The dependence of J_{sc} on electron fluence for Cell 2 is compared in Fig. III-7 with this dependence for the GaAs heteroface cell with Be doping and the Si nonreflective cell shown in Fig. III-5, and also with the dependence reported¹⁵ for a GaAs heteroface cell with Zn doping. As expected from theoretical considerations, the shallow-homojunction GaAs cell has a much smaller decrease in J_{sc} with increasing electron fluence.

Table III-1 also lists the device characteristics of Cells 3 and 4 (both on GaAs substrates) before and after 10^{16} e/cm^2 electron irradiation. The results for these cells are quite similar to those for Cell 1, except that they have lower initial η values because their n^+ -layers are thicker.

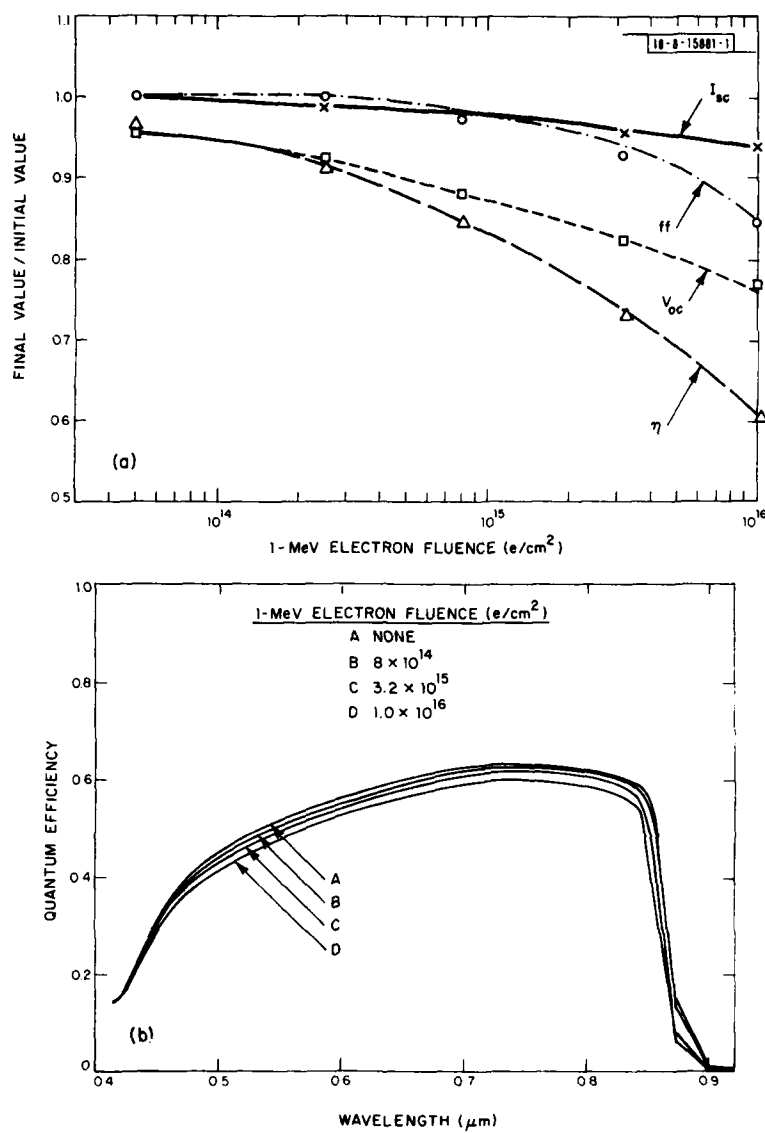


Fig. III-6. (a) Characteristics of Cell 2 as a function of cumulative electron fluence. (b) Quantum-efficiency data for Cell 2 after various electron exposures.

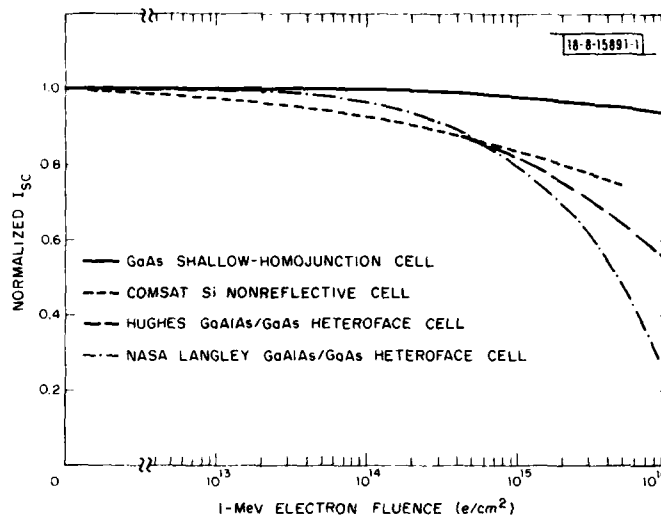


Fig. III-7. Normalized I_{sc} of Cell 2 as a function of cumulative electron fluence. Results for three other types of cells are also included. ($I_{sc} = J_{sc} \times \text{area}$.)

In conclusion, our experimental results for four $n^+/p/p^+$ shallow-homojunction GaAs solar cells indicate that such cells are resistant to electron irradiation. One of these cells is superior to other types of space cells, in having a higher output power density before and after $1 \times 10^{16} \text{ e/cm}^2$ 1-MeV electron irradiation. In a second cell, a very small change in J_{sc} was achieved by using a low doping level in the p-layer and no anodic AR coating. The still substantial change in V_{oc} may be partially attributable to an increase in leakage current along the exposed edges of our etched cell mesas. This increase in leakage current is expected to be reduced when the cell area is increased from 0.5 cm^2 to the usual value of 4 cm^2 , and when the exposed mesa edges are protected by an encapsulant. A different AR coating using Si_3N_4 is also being developed. By optimizing device design and fabrication procedure, it should be possible to obtain shallow-homojunction GaAs cells that will provide high power density and very long life in space.

In addition, our initial experiments indicate that shallow-homojunction GaAs cells fabricated on Ge substrates are similar to cells on GaAs substrates in their resistance to electron radiation. The substitution of Ge for GaAs substrates will permit a major decrease in Ga consumption as well as reduction in cell cost. Furthermore, since Ge is much stronger mechanically than GaAs, this substitution will also allow the use of thinner substrates, thus reducing the weight of the cells.

J. C. C. Fan
R. L. Chapman
C. O. Bozler

REFERENCES

1. J. C. C. Fan, C. O. Bozler, and R. L. Chapman, Appl. Phys. Lett. 32, 390 (1978), DDC AD-A058281/7.
2. C. O. Bozler, J. C. C. Fan, and R. W. McClelland, Chapter 5 in Gallium Arsenide and Related Compounds (St. Louis) 1978 (The Institute of Physics, London, 1979), pp. 429-436, DDC AD-A072370.
3. D. W. Shaw, J. Electrochem. Soc. 115, 405 (1968).
4. J. V. DiLorenzo, J. Cryst. Growth 17, 189 (1972).
5. L. Hollan and J. M. Durand, J. Cryst. Growth 46, 665 (1979).
6. J. M. Woodall and H. J. Hovel, J. Vac. Sci. Technol. 12, 1000 (1975).
7. J. J. Wysocki and P. Rappaport, J. Appl. Phys. 31, 571 (1960).
8. N. J. Nelson, K. K. Johnson, R. L. Moon, H. Y. Vander Plas, and L. W. James, Appl. Phys. Lett. 33, 26 (1978).
9. C. Stuerke, Conference Record of 13th IEEE Photovoltaic Specialists Conf., Washington, D.C., 5-8 June 1978, p. 551.
10. G. H. Walker, C. E. Byvik, E. J. Conway, J. H. Heinbockel, and M. J. Doviak, J. Electrochem. Soc. 125, 2034 (1978).
11. G. S. Kamath, J. Ewan, and R. C. Knechti, IEEE Trans. Electron. Devices ED-24, 473 (1977).
12. J. M. Woodall and H. J. Hovel, Appl. Phys. Lett. 30, 492 (1977).
13. A. Meulenbergh, D. J. Curtin, and R. W. Cool, Conference Record of 12th IEEE Photovoltaic Specialists Conf., Baton Rouge, Louisiana, 15-18 November 1976, p. 238.
14. S. Kamath and G. Wolff, Final Report on "High Efficiency GaAs Solar Cells," AFAPL-TR-78-96 (January 1979).
15. G. H. Walker and E. J. Conway, J. Electrochem. Soc. 125, 1726 (1978).

IV. MICROELECTRONICS

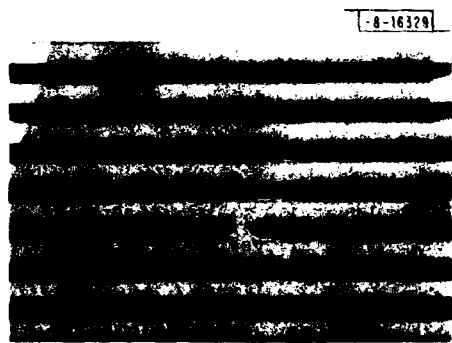
A. PHOTOLITHOGRAPHIC MASK EVALUATION BY ELECTRICAL TESTING

Previous reports have discussed methods and techniques for fabricating charge-coupled devices (CCDs).¹ Requirements for minimum attainable line width and spacing have increased the difficulties associated with 100-percent microscope inspection of chromium photolithographic masks. This report describes a DC measurement procedure which can assist in determining the presence of chromium bridges on metallization masks. These bridges would ultimately lead to intralevel shorts on completed silicon devices.

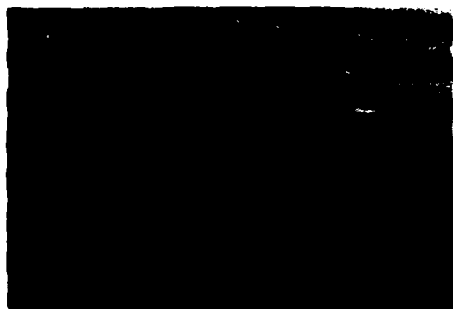
The GEODSS (Ground Electro-Optical Deep Space Surveillance) CCD imager [see Ref. 1, (1978:2), pp. 36-39] is characterized by a multiplicity of alternate-phase gate electrodes running horizontally along the imaging section of the device. As alternate gates are connected to different phases of the two-phase clock drive, a short between two adjacent electrodes on either the polycrystalline silicon first metallization level or the polycrystalline silicon second metallization level will render the device inoperative. These shorts can result from defects on the chromium photolithographic masks as well as from processing defects on the silicon wafer. To insure that mask defects between adjacent electrode lines are minimized, an electrical testing procedure which can reveal bridging defects has been developed.

Chromium-mask-making processes have been described previously.² The pattern on the final chromium master for a particular process level is the same as that which is to be replicated in polycrystalline silicon on the surface of the silicon wafer after development of positive photoresist and subsequent etching of unprotected areas. This mask consists of an array of devices closely packed within a 2-in. diameter, the same as the diameter of the silicon wafers. On the first polycrystalline silicon metallization level, the electrode width is 8.9 μm with conservative 6.3- μm spaces between adjacent electrodes. The second polycrystalline silicon level, however, consists of 11.4- μm -wide electrodes with 3.8- μm spaces between adjacent electrodes. With such narrow spacing between adjacent electrodes, gel slugs on the 10X emulsion reticle, particles on the mask before exposure, or incomplete development of the positive photoresist on the chromium-mask blank can result in shorts between electrodes. The imaging area on each chip is 3.0×12.2 mm. Stretched out, the adjacent electrodes of alternate phase would parallel one another over a length of 1.2 m. Since electrode gates of each phase are connected together at one side or the other of the 13.3×3.6 -mm chip, electrical probing of the 1200- \AA -thick pair of Cr electrode gate bus lines can reveal the presence of bridging shorts.

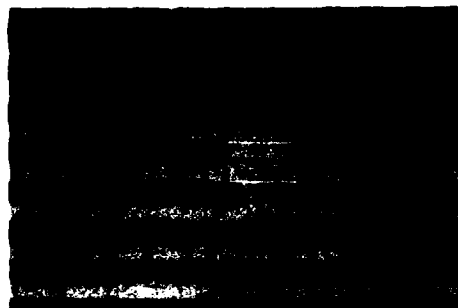
Figure IV-1(a) shows a typical bridging short on the GEODSS second-level metallization mask as seen under an inspection microscope; Fig. IV-1(b) shows this same defect after subsequent laser correction; and Fig. IV-1(c) shows a multiple-short defect. To detect these defects, DC I-V characteristics are measured on a transistor curve tracer. The presence of a short is characterized by a linear I-V line [Fig. IV-2(a)]. Typical single-bridge shorts have resistance between 60 and 80 k Ω . Multiple shorts such as that shown in Fig. IV-1(c) have resistance between 30 and 40 k Ω . An unusually high 1- to 10-M Ω resistance on some devices has also been noted [Fig. IV-2(b)]. This behavior corresponds to incomplete removal of chromium between alternate phase electrodes. This behavior does not necessarily indicate a defective die or mask, as this residual chromium film can be on the order of 20 to 70 \AA thick and still be relatively transparent to UV radiation.



(a)

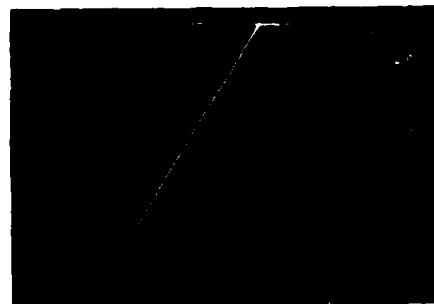


(b)



(c)

Fig. IV-1. Photomicrographs of second-level GEODSS metallization mask with 11.4- μ m lines and 3.8- μ m spacings. (a) Typical bridging defect between two adjacent metal lines; (b) same defect after correction by laser vaporization; (c) a lower-resistance multiple-metal-line short.



(a)



(b)

Fig. IV-2. Oscilloscope traces of shorts between adjacent metallization lines. (a) Typical I-V curve for multiple short of Fig. IV-1(c); (b) indicates high resistance characteristics typical of incompletely etched chromium.

Dice which indicate shorts are subsequently reinspected under a microscope to locate the defect. When the chromium bridging defect is located on the die, two techniques are available to remove the excess chromium. One method utilizes a focused Nd:YAG pulsed-laser beam to selectively vaporize the chromium bridging [Fig. IV-1(b)]. Another method involves the selective exposure of a small aperture in positive photoresist which has been applied to the defective masks. After development, the chromium bridge is etched off in chemical solution, and the remaining photoresist is stripped off.

D. J. Silversmith
R. W. Mountain

B. ENHANCED SUBSTRATE CONTACTS VIA LASER-ANNEALED BACK-SIDE ION IMPLANTATION INTO SILICON DEVICES

The jam-resistant, secure voice radio development program in the Tactical Systems Group is utilizing a 512-stage, binary-reference, analog CCD correlator chip.³ This chip is being developed and fabricated at a commercial development facility. Process design problems make these devices difficult to evaluate functionally as delivered, but by providing back-side ohmic contact to the device substrate, operation suitable for preliminary testing has been achieved. A technique has been developed using laser-annealed, back-side ion implantation to provide this contact without any damage to the aluminum metallization or glass passivation layers. This work demonstrates the feasibility of using laser annealing in combination with ion implantation for wafer rework at advanced stages of wafer fabrication, with the resulting increase in device yield.

Electrical testing of the correlator indicated that the summing busses were coupled to the clock on the CCD shift register, thus impairing device operation. A significant portion of the coupling problem was determined to result from nonohmic connection between the substrate pin on the package and the silicon substrate. Direct contact from the substrate pin on the package to the silicon substrate through the back of the device was not possible because the wafer backs were exposed to the same n^+ diffusions as the front for purposes of gettering heavy metal and alkali contaminants [see Ref. 1, (1977:4)].

Because the devices to be modified were received at the wafer probe stage (i.e., complete except for chip separation), the options for rework at Lincoln Laboratory were limited. The approach chosen was to make a direct ohmic contact from the ceramic dual-in-line package (DIP) die-attach pad to the silicon substrate. The first step in this process was the removal of the n^+ -layer on the back side by means of a CP4[†] etch while protecting the wafer front by cementing the wafer to a ceramic fixture with "black wax." The back side of the wafer was then implanted with boron at 10^{14} cm^{-2} at 100 keV. At this dose and energy, the implant damage is insufficient to drive the back surface amorphous. Because the temperatures required to activate this implant using thermal annealing would destroy the devices on the front of the wafer, a laser-annealing procedure^{4,5} was chosen for the electrical activation of the boron. An argon ion laser operating at 8 W CW output was focused to a 50- μm -diam spot on the wafer back. The wafer was scanned in a raster pattern under the beam on a servomechanical x-y stage such that nonoverlapping scans were made at 500- μm intervals. Scan rate of the stage was 4.3 cm/sec. After the laser scan was completed, the wafers were cleaned, and 300 Å of chromium and 1000 Å of gold were sequentially deposited from filaments in a vacuum evaporator. The gold was then electroplated to a thickness of 1 μm suitable for a gold-tin eutectic bond to the die attach pad of the ceramic DIP.

[†] $\text{HNO}_3\text{:HAc:HF}$ mixture.

Testing of the implanted, laser-annealed samples indicated resistances of 7 to 10 ohms between the forward-biased n^+ sources, drains, and diodes on a chip and the gold contact on the back. These values compare favorably with a calculated value of 5 ohms for a forward-biased n^+p diode with an equivalent area on a similar substrate material. Since only the boron in the 50- μm -wide laser-annealed stripes was electrically activated, this ohmic contact is obtained even though the ohmic-contact area is only 10 percent of the area of the back of the device. Devices from wafers with the ion-implanted, laser-annealed back-side ohmic contact have been eutectically bonded into the ceramic DIP and are operational. Several units have been delivered to the Tactical Systems Group for further evaluation.

In conclusion, the use of laser annealing for the activation of ion-implanted dopants in situations where conventional thermal processes are not possible has been demonstrated. Further, ion implantation coupled with laser annealing has been shown to be a tool for wafer rework at advanced stages of wafer fabrication, with the resulting improvement in yield and throughput.

D. J. Silversmith R. W. Mountain
S. C. Munroe M. W. Geis
(Group 41)

C. CHARGE-COUPLED DEVICES: IMAGERS

The CCD imaging devices currently fabricated for the GEODSS (Ground Electro-Optical Deep Space Surveillance) Program are required to have optical shielding to prevent illumination of the output register and detection circuitry. The only practical approach to this requirement is an opaque thin film integrated on the CCD chip. We describe here the use of the cermet film MgO/Au as an integrated-circuit light shield having the required features of high optical absorption, high resistivity, and ease of deposition and pattern definition.

Solid state imaging devices such as CCDs have transport registers which transfer the photo-generated charge from imaging cells to charge-detection circuitry. To avoid spurious signals, the transport registers and detection circuitry must be shielded from the illumination. If these features are sufficiently far removed from the imaging-cell array, a mechanical shield on the device package can solve the problem. More often, however, the features to be shielded are either too close to or interleaved with the imaging cells. In these cases, an integrated shield using a layer of aluminum on the device has been the common solution. A metallic film has two drawbacks when used in this manner, the more serious one being the additional capacitance which it introduces at the output charge collection diode. Additional stray capacitance at this node lowers the sensitivity of the detection circuit. The second problem which may occur is that light incident on the circuit near the edge of a reflecting film may, by multiple reflections between the substrate and the film, propagate laterally beneath the light shield. The ideal light shield would therefore be both an electrical insulator and highly absorbing for the radiation to which the imager is sensitive.

Cermet MgO/Au films prepared by RF sputtering from a target of 75-vol% MgO and 25-vol% Au have been investigated as selective black absorbers for use in solar collectors.^{5,6} The absorption coefficient for these films is about 10^5 cm^{-1} for wavelengths shorter than 1.1 μm . Thus, a 1- μm -thick film will have an optical density greater than 4 at all wavelengths for which silicon is sensitive. The resistivity of MgO/Au is about 100 ohm-cm when deposited on substrates at room temperature, but rises to over 10^4 ohm-cm if the substrate is held above 150°C.

At this resistivity, the RC time constants associated with the film and the SiO_2 layer covering the device beneath it are sufficiently long compared with CCD clock rates that capacitive loading by the film does not occur.

Because of possible radiation damage to the CCD due to the sputtering environment, we are investigating both ion-beam sputtering and RF diode sputtering as means of depositing MgO/Au films. While both systems generate UV radiation from the plasma near the target, the ion-beam system would not be expected to produce the high-energy electrons found in RF diode systems. The radiation damage commonly observed from these sources consists of an increase in both fixed positive oxide charge and fast interface state density. In the buried-channel CCDs used in these experiments, these effects manifest themselves as a shift in gate threshold voltage and an increase in dark current, respectively. In addition to CCDs, silicon wafers with a thin layer of thermal SiO_2 (800 Å) covered with Si_3N_4 (800 Å) to simulate the gate insulator of the CCD were also subjected to both deposition environments. For these wafers the MgO/Au was stripped, and MOS capacitors were fabricated and evaluated using MOS capacitance-voltage techniques.

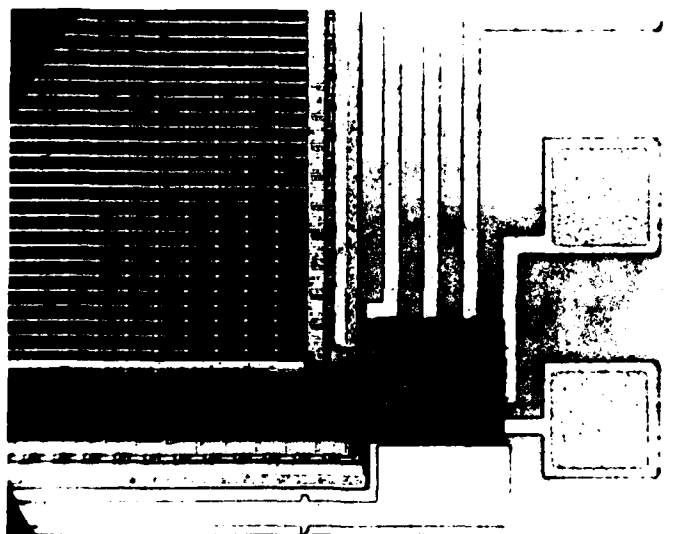


Fig. IV-3. Corner of GEODSS CCD imaging device showing black MgO/Au light shield covering output register and MOSFET detection circuit.

In the only run done thus far in a beam system (Fig. IV-3), a CCD wafer showed no change in threshold voltages or dark currents, and therefore no evidence of radiation damage insofar as CCD performance is concerned. However, the $\text{SiO}_2/\text{Si}_3\text{N}_4$ covered wafer did exhibit an increase in positive insulator charge and fast interface state density. This discrepancy is likely due to the fact that additional layers present on the CCD, particularly the overlapping two-level polysilicon gate structure, shield the CCD channel from the UV radiation. In the RF sputtering system at power levels of 30 to 40 W, a similar difference has been seen, but with the exception that an increase in dark current from about $4 \text{ nA}/\text{cm}^2$ to about $50 \text{ nA}/\text{cm}^2$ after deposition was

observed in the CCDs. However, by annealing the CCD wafer in N_2 at $300^\circ C$ for 30 min., the dark currents were reduced close to their initial values. Although both deposition methods are promising, future work will emphasize the ion-beam method since it appears to subject a CCD to less radiation damage.

B. E. Burke
F. J. Bachner
J. C. C. Fan

REFERENCES

1. Solid State Research Reports, Lincoln Laboratory, M.I.T. (1976:1), pp. 59-62, DDC AD-A027261/7; (1977:2), pp. 47-49, DDC AD-A044795; (1977:4), pp. 46-47, DDC AD-A052463/7; and (1978:2), pp. 40-43, DDC AD-A061241/6.
2. Ibid. (1977:3), pp. 39-42, DDC AD-A050551/1.
3. D. A. Gandolfo et al., IEEE Trans. Electron Devices ED-26, 596 (1979).
4. S. D. Ferris, H. J. Leamy, and J. M. Poole, Eds., Laser-Solid Interactions and Laser Processing - 1978, AIP Conference Proceedings No. 50 (American Institute of Physics, New York, 1979).
5. J. C. C. Fan and P. M. Zavracky, Appl. Phys. Lett. 29, 478 (1976), DDC AD-A037629/3.
6. J. C. C. Fan, Thin Solid Films 54, 139 (1978), DDC AD-A069423.

V. ANALOG DEVICE TECHNOLOGY

A. EFFICIENT CONVERSION OF SURFACE ACOUSTIC WAVES IN SHALLOW GRATINGS TO BULK PLATE MODES

During recent measurements of the slowing of surface acoustic waves (SAWs) due to transmission through shallow groove gratings,¹ a novel phenomenon was observed. The transmission response showed a series of very narrow stop bands for surface waves normally incident on 200-groove gratings. The frequency range of the observed stop bands extends ± 20 percent around the frequency at which the SAW wavelength equals the groove period. At these stop bands, the grating converts the surface wave to a slab waveguide mode. Resonant coupling results in sharp resonant stop bands.

Sharp passbands are, however, of more practical interest than sharp stop bands. This led us to seek access to the signal that is taken out in the stop bands. Here, we report passbands observed by means of a second grating on the bottom of the crystal, present briefly a theory which accounts for the resonance phenomenon in terms of bulk plate modes, and suggest structures which may result in practical devices.

A cross section of the structure used is shown schematically in the upper-left corner of Fig. V-1. The substrate is a slab of 1.27-mm-thick YZ LiNbO_3 with polished faces. Both gratings have 200 grooves with 20.32- μm period and 0.47- μm depth. The gratings are 2.29 mm wide.

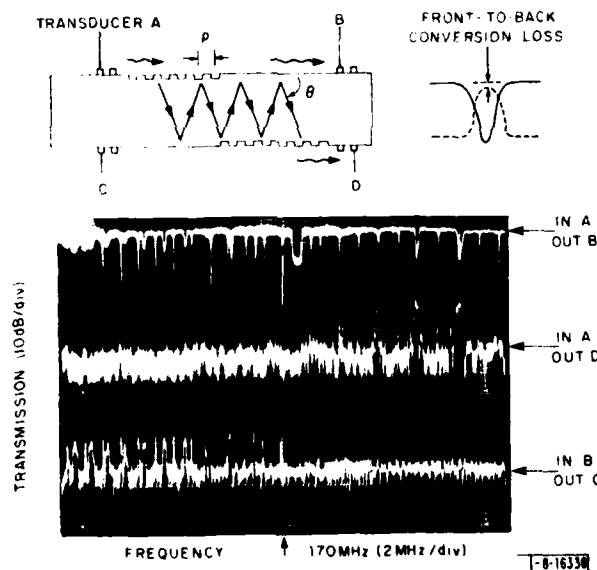


Fig. V-1. Surface-to-bulk-wave coupling. Top left: Schematic of cross section of substrate. For case of input at A, bulk waves are shown bouncing from top to bottom in "ray-tracing" view of plate mode (Ref. 1). Lower left is composite photo of frequency response measured for paths indicated. Central trace is displaced 30 dB down with respect to upper one. When they are at same gain, conversion loss is measured as shown at top right. Bottom trace is at same gain as central one but pictorially displayed 6 divisions lower.

All transducers have 2-1/2 finger pairs. The gratings are offset so that the last groove of the upper one is approximately over the first groove of the lower one.

Traces of log transmission vs frequency are shown in Fig. V-1. For input and output on the same surface (A-to-B or C-to-D), sharp and deep stop bands are observed. For input and output on opposite surfaces (A-to-D or B-to-C), passbands are observed at the positions of these stop bands. The signal in some of these passbands is nearly of the same level as the signal on either side of the corresponding stop bands. Since the transducers in the various paths are identical and can be assumed to have the same loss, the front-to-back transmission loss can be measured by superposing the traces as shown in the upper right of Fig. V-1. A detailed examination of the passband levels on two such structures showed that for some of the bands the conversion loss was zero within a measurement accuracy of ± 0.5 dB, while for others a few decibels of loss was observed.

The theoretical analysis was aimed at the calculation of the frequencies of the stop bands and/or passbands, and the magnitudes of the peaks in the transfer function between the two gratings. The theory briefly outlined here, and to be published in detail elsewhere,² starts from a mode-coupling formalism.³ The Rayleigh wave of propagation constant k_r couples, via the grating of periodicity p , to a slab waveguide mode. In an isotropic slab, near cutoff, the coupling between shear and compressional waves is weak, and the propagation constant k_w of the slab waveguide modes follows quite closely the approximate dispersion curves

$$k_w = \left[\left(\frac{\omega}{c_s} \right)^2 - \left(\frac{n\pi}{d} \right)^2 \right]^{1/2} \quad \text{and} \quad k_w = \left[\left(\frac{\omega}{c_c} \right)^2 - \left(\frac{m\pi}{d} \right)^2 \right]^{1/2} \quad (\text{V-1})$$

where c_s and c_c are the speeds of the shear and compressional waves, and d is the thickness of the slab. In the slab, the mode orders n and m are close to 100 and 60, respectively. Whenever the synchronism condition

$$k_r - \frac{2\pi}{p} = k_w \quad (\text{V-2})$$

is obeyed, maximum interaction occurs between the Rayleigh wave and the bulk wave. Figure V-2 shows a dispersion diagram for the Rayleigh wave shifted by $2\pi/p$, and for the slab waveguide modes. Strong interaction occurs when the respective dispersion curves cross, as indicated in Eq. (V-2). The frequencies of the stop bands or of the transmissions between top and bottom were determined from the crossings, as in Fig. V-2, and were found to agree reasonably well with the experimentally observed ones. The small deviations are probably due to the fact that anisotropy and shear-to-compression-wave coupling are neglected.

At frequencies higher than the critical frequency $f_c = c_r/p$, the grating excites a slab mode that propagates in the same direction; at frequencies below the critical frequency, oppositely directed slab modes are excited. Thus, in Fig. V-1, A-to-D passbands are observed only above the experimental $f_c = 171.5$ MHz and B-to-C passbands only below f_c .

Coupling between waves with group velocities in the same direction leads to spatial intensity distributions that are quite different than the distributions which result from coupling between waves of oppositely directed group velocities. In the former case, the coupling leads to a spatial beat between the two coupled waves; the power in one wave gets transferred to the other, but is returned to the first wave if the transition length (as measured in terms of the coupling constant) is sufficiently long. In the latter case of oppositely directed group velocities, no spatial beat occurs. The coupling of one wave to the other is a monotonically increasing function

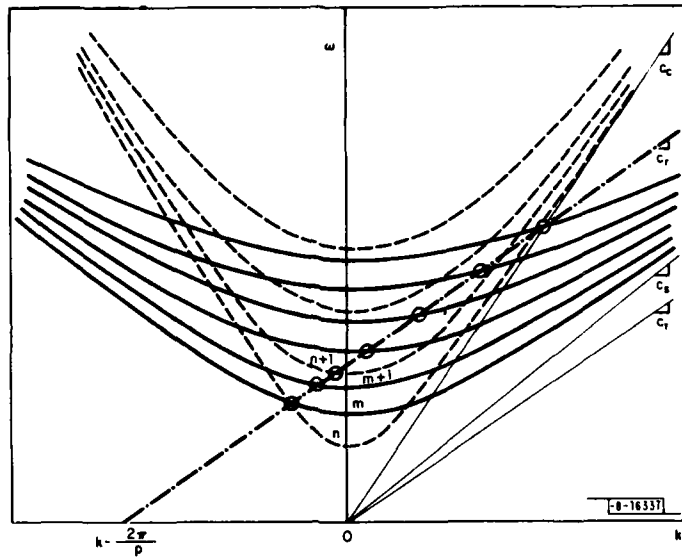


Fig. V-2. Dispersion diagram for shear (solid hyperbolas) and compressional (dashed hyperbolas) slab modes, and for shifted Rayleigh wave (dot dash) and unshifted Rayleigh wave (solid line of slope c_T). For large k , slab modes approach bulk-wave asymptotes c_{Sk} and c_{Ck} . Synchronism conditions are satisfied at intersection indicated with "0" and determine frequencies of observed passbands. Since $c_T < c_S < c_C$, there is no conversion between SAW and bulk power without a grating.

of length and/or coupling constant. Further, the coupling constant κ is inversely proportional to the square root of the group velocities of the waves. The slab modes have group velocities that decrease to zero as cutoff is approached. Hence, one gathers that the coupling κL within a grating of length L increases monotonically with decreasing $|\omega - \omega_c|$ ($\omega_c = 2\pi f_c$). Traces such as in Fig. V-1, particularly when seen on a compressed scale over wider bandwidth, show trends in agreement with the mode-coupling formalism. For $\omega < \omega_c$, one sees two sets of stop-band spikes — one for the compressional slab waves (more widely spaced), the other for shear waves; both increase as one moves toward ω_c . For $\omega > \omega_c$, the behavior is more irregular in that the transfer of power from the surface wave is not a monotonically increasing function of κL .

Several device structures can be envisaged based on this surface-to-bulk and bulk-to-surface-wave conversion. One of the simplest is a bandpass filter with the signal traveling in a U path as shown in Fig. V-3. The grating period p_1 is slightly larger than the acoustic

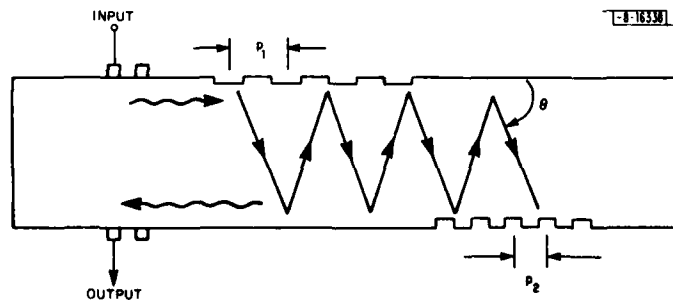


Fig. V-3. Schematic of crystal cross section of proposed U-path filter.

wavelength, so that the bulk wave is launched forward ($\theta < 90^\circ$). The grating period p_2 is slightly smaller than the wavelength so that coupling is to the backward surface wave on the bottom. This device would display a single passband. The periods p_1 and p_2 must be chosen using the above theory. They will depend on the desired center frequencies, on the crystal thickness, and on the bulk and surface-wave velocities.

The present work demonstrates that gratings can efficiently shift a surface wave from one to another surface of an acoustic slab via the plate mode. The device suggested, or others one can think of, may offer an opportunity to use some of the advantages of bulk waves such as lower loss, compactness, and insensitivity to surface aging, and still maintain planar, albeit two-surface, fabrication.

J. Melngailis
H. A. Haus[†]
A. Lattes[†]

B. FABRICATION OF JOSEPHSON-JUNCTION DEVICES

Techniques have been developed for the fabrication and testing of Josephson-junction devices.⁴ The basic device structure is a niobium/niobium oxide/lead sandwich, as sketched in Fig. V-4, with niobium and lead serving as the superconducting electrodes and niobium oxide as a tunneling barrier. The use of niobium as the base film produces stable and reliable devices.⁵ This is due, in large part, to the extreme stability and ruggedness of the niobium and niobium oxide films. The high critical temperature of niobium relative to other elemental superconductors is another of its advantages. However, the high relative dielectric constant (~ 30) of niobium oxide tends to reduce the switching speed of these junctions.

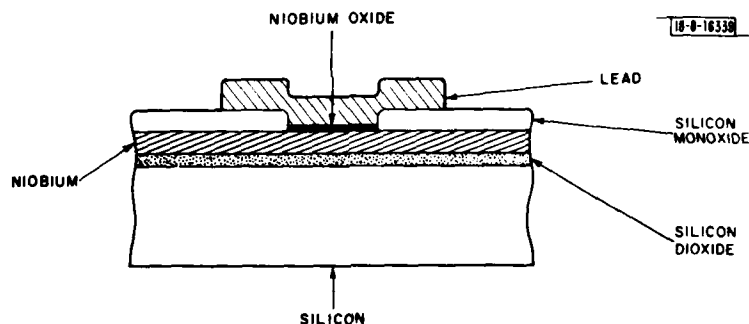


Fig. V-4. Josephson tunnel junction.

The Nb is deposited on oxidized silicon wafers by RF sputtering in an argon atmosphere. Critical transition temperatures for the $0.4\text{-}\mu\text{m}$ -thick films are within several tenths of degrees of the bulk value (9.4 K).

A reactive-ion-etching process has been implemented for the delineation of desired patterns in the Nb and SiO films. Standard photolithography is used to generate a pattern in positive photoresist on top of the film. The resist then serves as the mask for the highly directive etching. The reactive gas species and operating parameters have been optimized for the selectivity and uniformity of the etching process. The $1\text{-}\mu\text{m}$ resolution currently being realized is limited by the photolithography rather than the etching process.

[†] Research Laboratory for Electronics, M.I.T.

The most critical process step is the realization of uniform and reproducible tunnel barriers between the two superconducting electrodes. A native oxide tunnel barrier is grown on the Nb surface by an RF plasma-oxidation procedure developed by Greiner.⁶ With this procedure the exposed Nb surface is simultaneously sputtered and oxidized in an O_2/Ar plasma. In principle it is possible to reach a plateau in which oxide growth is balanced against oxide removal, and oxide thickness becomes independent of oxidation time. The realization of reproducible tunnel barriers depends upon careful control of parameters which affect the sputtering and oxidation rates, such as the partial pressure of oxygen, sputtering voltages, and temperature.

After formation of the oxide barrier, and without breaking vacuum, the counter electrode, a 0.6- μm -thick layer of Pb (or Pb/Bi) is evaporated over the entire surface of the wafer. A photoresist mask is then fabricated and the Pb layer is patterned by chemical etching. The tendency of pure Pb films to form large grains and hillock structures currently limits the resolution of the Pb etching process to about 6 μm . Hillock growth can be prevented by adding small portions of an impurity to the pure Pb.⁷ One such alloy, Pb-Bi, is currently being explored for use in the Nb-based junctions. Such junctions have been fabricated and reasonable current-voltage characteristics obtained.

Both Al and an In-Au alloy⁸ have been explored as resistive materials in the superconductive circuitry. In terms of their resistance vs temperature characteristics, both materials are reasonably well behaved between 273 and 4.2 K. Al appears to make reasonable contacts with Nb films, while the In-Au alloy is more compatible with Pb or Pb alloys. An Al/Nb metallization is currently being employed as pads for an ultrasonic-bonding process.

The current-voltage characteristic of a Nb/Nb₂O₅/Pb Josephson junction is shown in Fig. V-5. With zero potential across the tunnel barrier, the DC Josephson current will flow up to some critical level (I_c). When the junction current exceeds I_c , the potential across the junction will switch to a nonzero value. For nonzero potentials below the sum of the half-energy gaps (Δ_{Nb}, Δ_{Pb}), the dominant current is due to tunneling of normal electrons (quasi-particles) and to microshorts or other conduction mechanisms which can produce an anomalous "excess current."

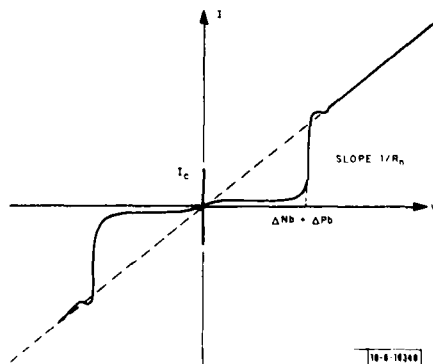


Fig. V-5. Sketch of I-V characteristic of a superconductive tunnel junction (Nb-Nb₂O₅-Pb) at 4.2 K.

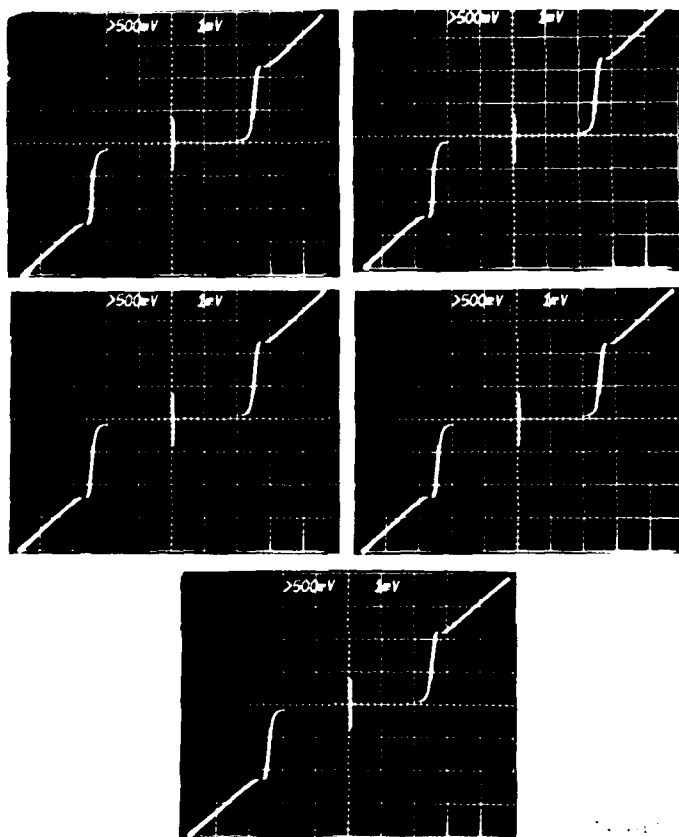


Fig. V-6. I-V characteristics of five adjacent (0.35-cm centers) superconductive tunnel junctions ($\text{Nb-Nb}_x\text{O}_y\text{-Pb}$). (Horizontal scale: 1 mV/div; vertical scale: 5 mA/div.)

Junction resistance R_n decreases exponentially with oxide thickness. For Nb-based junctions, an increase in the oxide barrier of only 4 Å can produce an order-of-magnitude decrease in tunnel current. Using the Greiner RF plasma-oxidation method, arrays of junctions are being produced whose resistances R_n vary by less than 20 percent. For example, the values for R_n of the junctions shown in Fig. V-6 vary by less than 10 percent, corresponding to oxide barrier thicknesses uniform to a fraction of an angstrom.

In summary, technology has been established for fabricating devices with five basic layers: (1) Nb base electrode, (2) SiO insulator, (3) Pb counter electrode, (4) resistors and connectors, and (5) bonding-pad metallization. The need exists to improve the resolution of the Pb-patterning process and to add one or more additional superconductive layers to serve as a ground plane and for inductive coupling to Josephson circuit loops. A Josephson device for analog-signal processing is currently under development.

S. A. Reible

REFERENCES

1. J. Melngailis and R. C. Williamson, 1978 Ultrasonics Symposium Proceedings (IEEE, New York, 1978), p. 623, DDC AD-A069931.
2. H. A. Haus and A. Lattes, "Coupling Between SAW Grating and Bulk Waves," Research Laboratory of Electronics Report, M.I.T. (n.d.); and H. A. Haus, A. Lattes, and J. Melngailis (in preparation).
3. W. H. Louisell, Coupled Modes and Parametric Electronics (Wiley, New York, 1960).
4. B. D. Josephson, Adv. Phys. **14**, 419 (1965).
5. L. S. Hoel, W. H. Keller, J. E. Nordman, and A. C. Scott, Solid-State Electron. **15**, 1167 (1972).
6. J. H. Greiner, J. Appl. Phys. **42**, 5151 (1971).
7. S. K. Lahiri, J. Vac. Sci. Technol. **13**, 148 (1976).
8. S. K. Lahiri, "Thin Film Resistors and Contacts for Circuitry," 1975, United States Patent No. 3,913,120.

UNCLASSIFIED

SECURITY CLASSIFICATION OF THIS PAGE (When Data Entered)

19 REPORT DOCUMENTATION PAGE		READ INSTRUCTIONS BEFORE COMPLETING FORM
1. REPORT NUMBER 18 ESD-TR-79-218	2. GOVT ACCESSION NO. AD-A084270	3. RECIPIENT'S CATALOG NUMBER
4. TITLE (and Subtitle) 6 Solid State Research, 1979:3.		5. TYPE OF REPORT & PERIOD COVERED 9 Quarterly Technical Summary 1 May - 31 July 1979 rept.
7. AUTHOR(s) 10 Alan L. McWhorter		6. PERFORMING ORG. REPORT NUMBER 1979:3
9. PERFORMING ORGANIZATION NAME AND ADDRESS Lincoln Laboratory, M.I.T. P.O. Box 73 Lexington, MA 02173		8. CONTRACT OR GRANT NUMBER(s) 15 F19628-78-C-0002
11. CONTROLLING OFFICE NAME AND ADDRESS Air Force Systems Command, USAF Andrews AFB Washington, DC 20331		10. PROGRAM ELEMENT, PROJECT, TASK AREA & WORK UNIT NUMBERS Program Element No. 65705F Project No. 649L
14. MONITORING AGENCY NAME & ADDRESS (if different from Controlling Office) Electronic Systems Division Hanscom AFB Bedford, MA 01731		12. REPORT DATE 11 15 August 1979
16. DISTRIBUTION STATEMENT (of this Report) Approved for public release; distribution unlimited.		13. NUMBER OF PAGES 76
17. DISTRIBUTION STATEMENT (of the abstract entered in Block 20, if different from Report)		15. SECURITY CLASS. (of this report) Unclassified
18. SUPPLEMENTARY NOTES None		15a. DECLASSIFICATION DOWNGRADING SCHEDULE
19. KEY WORDS (Continue on reverse side if necessary and identify by block number)		
solid state devices quantum electronics materials research microelectronics	analog device technology photodiode devices lasers laser spectroscopy	imaging arrays infrared imaging surface-wave transducers
20. ABSTRACT (Continue on reverse side if necessary and identify by block number)		
<p>This report covers in detail the solid state research work of the Solid State Division at Lincoln Laboratory for the period 1 May through 31 July 1979. The topics covered are Solid State Device Research, Quantum Electronics, Materials Research, Microelectronics, and Analog Device Technology. Funding is primarily provided by the Air Force, with additional support provided by the Army, ARPA, NSF, and DOE.</p> <p style="text-align: right;">207650 24</p>		

DD FORM 1 JAN 73 1473 EDITION OF 1 NOV 65 IS OBSOLETE

UNCLASSIFIED

SECURITY CLASSIFICATION OF THIS PAGE (When Data Entered)